

# AMICO galaxy clusters in KiDS-DR3: cosmological constraints from large-scale stacked weak lensing profiles

Carlo Giocoli<sup>1,2,3,\*</sup>, Federico Marulli<sup>2,1,3</sup>, Lauro Moscardini<sup>2,1,3</sup>, Mauro Sereno<sup>1,3</sup>, Alfonso Veropalumbo<sup>4,5</sup>, Lorenzo Gigante<sup>2</sup>, Matteo Maturi<sup>6,7</sup>, Mario Radovich<sup>8</sup>, Fabio Bellagamba<sup>2</sup>, Mauro Roncarelli<sup>2</sup>, Sandro Bardelli<sup>1</sup>, Sofia Contarini<sup>2,1</sup>, Giovanni Covone<sup>9,10,11</sup>, Joachim Harnois-Déraps<sup>12,13</sup>, Lorenzo Ingoglia<sup>9</sup>, Giorgio F. Lesci<sup>2,1</sup>, Lorenza Nanni<sup>2,14</sup>, Emanuella Puddu<sup>10</sup>

<sup>1</sup> INAF - Osservatorio di Astrofisica e Scienza dello Spazio di Bologna, via Gobetti 93/3, I-40129 Bologna, Italy

<sup>2</sup> Dipartimento di Fisica e Astronomia "Augusto Righi", Alma Mater Studiorum Università di Bologna, via Gobetti 93/2, I-40129 Bologna, Italy

<sup>3</sup> INFN - Sezione di Bologna, viale Berti Pichat 6/2, I-40127 Bologna, Italy

<sup>4</sup> Dipartimento di Fisica, Università degli Studi Roma Tre, via della Vasca Navale 84, I-00146 Rome, Italy

<sup>5</sup> INFN - Sezione di Roma Tre, via della Vasca Navale 84, I-00146 Rome, Italy

<sup>6</sup> Zentrum für Astronomie, Universität Heidelberg, Philosophenweg 12, D-69120 Heidelberg, Germany

<sup>7</sup> ITP, Universität Heidelberg, Philosophenweg 16, D-69120 Heidelberg, Germany

<sup>8</sup> INAF - Osservatorio Astronomico di Padova, vicolo dell'Osservatorio 5, I-35122 Padova, Italy

<sup>9</sup> Dipartimento di Fisica "E. Pancini", Università di Napoli Federico II, C.U. di Monte Sant'Angelo, via Cintia, I-80126 Napoli, Italy

<sup>10</sup> INAF - Osservatorio Astronomico di Capodimonte, Salita Moiariello 16, I-80131, Napoli, Italy

<sup>11</sup> INFN - Sezione di Napoli, via Cintia, I-80126, Napoli, Italy

<sup>12</sup> Astrophysics Research Institute, Liverpool John Moores University, 146 Brownlow Hill, Liverpool, L3 5RF, UK

<sup>13</sup> School of Mathematics, Statistics and Physics, Newcastle University, Herschel Building, NE1 7RU Newcastle-upon-Tyne, United Kingdom

<sup>14</sup> Institute of Cosmology & Gravitation, University of Portsmouth, Dennis Sciama Building, Portsmouth, PO1 3FX, UK

2021

## ABSTRACT

**Context.** The large-scale mass distribution around dark matter haloes hosting galaxy clusters provides sensitive cosmological information.

**Aims.** In this work, we make use of a large photometric galaxy cluster sample, constructed from the public Third Data Release of the Kilo-Degree Survey, and the corresponding shear signal, to assess cluster masses and test the concordance  $\Lambda$ -cold dark matter ( $\Lambda$ CDM) model. In particular, we study the weak gravitational lensing effects on scales beyond the cluster virial radius, where the signal is dominated by correlated and uncorrelated matter density distributions along the line-of-sight. The analysed catalogue consists of 6962 galaxy clusters, in the redshift range  $0.1 \leq z \leq 0.6$  and with signal-to-noise ratio larger than 3.5.

**Methods.** We perform a full Bayesian analysis to model the stacked shear profiles of these clusters. The adopted likelihood function considers both the small-scale 1-halo term, used primarily to constrain the cluster structural properties, and the 2-halo term, that can be used to constrain cosmological parameters.

**Results.** We find that the adopted modelling is successful to assess both the cluster masses and the total matter density parameter,  $\Omega_M$ , when fitting shear profiles up to the largest available scales of 35 Mpc/h. Moreover, our results provide a strong observational evidence of the 2-halo signal in the stacked gravitational lensing of galaxy clusters, further demonstrating the reliability of this probe for cosmological studies. The main result of this work is a robust constraint on  $\Omega_M$ , assuming a flat  $\Lambda$ CDM cosmology. We get  $\Omega_M = 0.29 \pm 0.02$ , estimated from the full posterior probability distribution, consistent with the estimates from cosmic microwave background experiments.

**Key words.** Galaxy Clusters - Observational Cosmology - KiDS-DR3 Survey - Stacked Weak Lensing - Cluster Mass Inference - Cosmological parameters inference

## 1. Introduction

The standard  $\Lambda$ -cold dark matter ( $\Lambda$ CDM) cosmological model provides the most convenient and simplest parametrisation of the so-called Concordance Model. Recent wide field observational surveys have provided stringent constraints about the two most contributing energy-density constituents of our Universe: the dark energy and the dark matter. While the first contributes

to about  $\sim 68\%$  of the total mass-energy, the latter constitutes about  $\sim 27\%$  (Bennett et al. 2013; Planck Collaboration et al. 2014; Planck Collaboration 2016; Planck Collaboration et al. 2020). The current consensus view is that this dark matter component is mainly cold, being composed of particles moving at non-relativistic speeds. Only  $\sim 5\%$  of the Universe is made up of ordinary matter (baryons), and even less of radiation ( $\sim 10^{-5}$ ).

The  $\Lambda$ CDM model is not based on any particular assumption about the nature and physical origin of the dark components.

\* email: [carlo.giocoli@inaf.it](mailto:carlo.giocoli@inaf.it)

Nevertheless, it is currently the best cosmological model available to describe the large-scale structure of the Universe and its evolution. Moreover, different observations (Hikage et al. 2019; Hamana et al. 2020; Bautista et al. 2021) show that the geometry of our Universe is flat on large scales, so that the Concordance Model is often also called the flat  $\Lambda$ CDM model.

In this scenario, clusters of galaxies play an important role both for constraining cosmological parameters (Sheth & Tormen 1999; Tormen 1998; Borgani & Kravtsov 2011), and for the study of the formation and evolution of the galaxies in their environment (Springel et al. 2001b; Borgani et al. 2004; Andreon 2010; Angulo et al. 2012; Zhang et al. 2016; Zenteno et al. 2016). In fact, galaxy clusters are hosted by the most massive virialised CDM haloes, and their redshift evolution – number density and spatial distribution – is highly sensitive to different cosmological parameters (see e.g. Planck Collaboration et al. 2016; Vikhlinin et al. 2009; Veropalumbo et al. 2014, 2016; Sereno et al. 2015; Pacaud et al. 2018; Marulli et al. 2018, 2020; Costanzi et al. 2019; Moresco et al. 2020; Lesci et al. 2020; Nanni et al. prep).

By exploiting the optical and near infrared bands, it is possible to identify clusters by searching for the cluster-scale overdensities in the three-dimensional galaxy distribution of wide field observations. This technique allows to cover large and deep areas of the sky through photometric surveys, giving the possibility to collect a sufficiently large number of clusters and use them as cosmological tool. Ongoing and planned photometric surveys will allow us to increase by orders of magnitude the present census of galaxy clusters, expanding their detection toward lower masses and higher redshifts (LSST Science Collaboration et al. 2009; Laureijs et al. 2011; Spergel et al. 2013; Sartoris et al. 2016).

However, in order to use galaxy clusters as probe to infer cosmological parameters it is crucial to derive precise and reliable cluster mass estimates (Meneghetti et al. 2010b; Giocoli et al. 2014). In particular, the measured number of galaxy cluster members, accessible in photometric or spectroscopic observations, are typically used as mass-proxy, to be linked to the total mass of the cluster (Simet et al. 2017; Murata et al. 2019). Calibrating the relationship between mass-proxy and the true three-dimensional mass is often challenging and sometime hidden in complex, and not yet well understood, astrophysical processes (Rasia et al. 2012, 2013; Angelinelli et al. 2020).

The most reliable approach to estimate cluster masses is currently provided by the gravitational lensing signal on background galaxies (Bartelmann & Schneider 2001; Umetsu 2020). The robustness of this method relies on the fact that it does not require any assumption on the dynamical state of the luminous and dark matter, being sensitive only to the total projected matter density distribution between the sources and the observer. In particular, the weak lensing effect consists of slight distortions of the source shapes (called shear) and the intensification of their apparent brightness (magnification), caused by the deflection and the convergence of light rays travelling from the sources to the observer. The weak lensing comes into play when the source is at large angular distances from the geometric centre of the lens. Hence it is also very useful to probe the lensing cluster profiles up to large radii. All of these properties made the weak lensing extremely powerful to probe the mass density distributions in clusters on different scales (Sereno et al. 2018).

A small number of background galaxies limits the study of individual cluster masses down to few times  $10^{14} M_{\odot}$  for typical current optical surveys. Indeed, in order to reach a large signal-to-noise in the weak lensing mass estimate, it is a com-

mon practice to stack the weak lensing signal – averaging the number of slightly distorted galaxy images in radial bins to increase the shear estimate and reduce the noise – of systems in the same redshift and observable bins: the resultant signal is that of the mass-weighted ensemble. Precisely, the stacked gravitational lensing represents the cross-correlation between foreground deflector positions and background galaxy shears. Given a shallow but broad survey, stacking the signal around a large number of lenses is an efficient method to compensate for the low number density of lensed sources. For example, this approach was applied with great success to the Sloan Digital Sky Survey (SDSS) data to measure the ensemble averaged lensing signal around groups and clusters (Mandelbaum et al. 2006; Sheldon et al. 2009). By splitting the sample of clusters into subsets based on an observable property, such as amplitude or optical richness, it is possible to determine the scaling relations between the observable and the mean mass of the sample (see, e.g., Bellagamba et al. 2019).

In this work we will exploit the data-set from the Kilo Degree Survey (KiDS hereafter) (de Jong et al. 2013). The principal scientific goal of KiDS is to exploit the weak lensing and photometric redshift measurements to map the matter large-scale distribution in the Universe.

Appropriate algorithms have to be used to identify galaxy clusters in photometric surveys. In this work we exploit the Adaptive Matched Identifier of Clustered Objects (AMICO) algorithm, presented and tested in Bellagamba et al. (2018), and used to extract the cluster sample from KiDS-DR3 by Maturi et al. (2019). AMICO is an algorithm for the detection of galaxy clusters in photometric surveys where the data-set is affected by a noisy background. It is built upon a linear optimal matched filter method (Maturi et al. 2005, 2007; Viola et al. 2010; Bellagamba et al. 2011), which maximises the signal-to-noise ratio ( $S/N$ ) taking advantage of the statistical properties of the field and cluster galaxies.

We build the shear profile of our lens samples following the conservative approach detailed in (Bellagamba et al. 2019), then stack the profile signal to increase the  $S/N$ . We determine the weighted ellipticity of the background sources in radial bins, that is the tangential and cross components of the shear. In our subsequent analyses we use only the tangential component. Hence are effectively measuring the shear-cluster correlation function.

For most of the clusters in the sample, the  $S/N$  in the shear data is too low to constrain the density profile and, consequently, to measure a reliable mass. So we are tied to measure the mean mass for ensembles of objects chosen according to their observables and redshift. In short words, we exploit the shear-cluster correlation (or stacked lensing).

The main goal of this work is to assess both the cluster masses and the total matter density parameter,  $\Omega_M$ , modelling the shear-cluster correlation up to the largest available scales.

The statistical numerical code has been built with the CosmoBoLognaLib (V5.3), a set of *free software* C++/Python libraries (Marulli et al. 2016) that provide all the functions used for the estimation of the various cosmological components of our fitting model.

This work is organised as follows. In Sec. 2 we present the observational data-set: shear and cluster catalogues. We introduce our theoretical model in Sec. 3, that we adopt to describe the stacked tangential shear profile of the cluster sample. In Sec. 4 we display our results, then summarise and conclude in Sec. 5.

In all the analyses presented in this work, we assume a flat  $\Lambda$ CDM model with baryon density  $\Omega_b = 0.0486$  and scaled Hub-

ble parameter  $h = 0.7$ . The matter density parameter is left free except in the first analysis stage where, to infer reference cluster masses while modelling the 1-halo term, it is fixed to  $\Omega_M = 0.3$ . When inferring  $\Omega_M$  from the 2-halo modelling, we assume anyway a flat  $\Lambda$ CDM, hence  $\Omega_\Lambda = 1 - \Omega_M$  is a derived parameter. The symbol  $\log$ , if not specified otherwise, refers to the logarithm base 10 of the quantity.

## 2. Data

KiDS (de Jong et al. 2013) is an optical wide-field imaging survey aiming at mapping 1350 square degrees of extra-galactic sky in two stripes (an equatorial one, KiDS-N, and one centred around the South Galactic Pole, KiDS-S) in four broad-band filters ( $u, g, r, i$ ). The observations are performed with the 268 Megapixels OmegaCAM wide-field imager (Kuijken 2011), owning a mosaic of 32 science CCDs and positioned on the Very Large Telescope (VLT) Survey Telescope (VST). This is an ESO telescope of 2.6 meters in diameter, located at the Paranal Observatory (for further technical information about VST see Capaccioli & Schipani 2011). The principal scientific goal of KiDS is to exploit weak lensing and photometric redshift measurements to map the large-scale matter distribution in the Universe. The VST-OmegaCAM is an optimal choice for such a survey, as it was expressly created to give excellent and uniform image quality over a large ( $1 \text{ deg}^2$ ) field of view with a resolution of 0.21 arcsec/pixel. Note that a field of view  $1 \text{ deg}$  wide corresponds to  $\sim 12.5 \text{ Mpc}/h$  at the median redshift of our lens sample,  $z \sim 0.35$ .

The DR3-KiDS catalogue is composed of about 100,000 sources per square degree, for a total of almost 50 million sources over the full survey area. These data are attentively and uniformly calibrated and made usable in an easily accessible dedicated archive.

We exploit the Third Data Release survey (KiDS-DR3, de Jong et al. 2017), which has been obtained with the same instrumental settings of the other two previous releases (de Jong et al. 2015) that were made public in 2013 (DR1) and 2015 (DR2). KiDS-DR3 extends the total released data-set coverage to approximately  $447 \text{ deg}^2$  with 440 survey tiles. Therefore, with respect to the other previous releases, it provided a considerable survey area extension. This release also includes photometric redshifts with the corresponding probability distribution functions, a global improved photometric calibration, weak lensing shear catalogues and lensing-optimised image data. Source detection, positions and shape parameters used for weak lensing measurements are all derived from the stacked  $r$ -band images, while magnitudes are measured in all filters using forced photometry.

One of the main improvements of KiDS-DR3, compared to DR1 and DR2, is the enhanced photometric calibration and the inclusion of photometric redshift distribution probabilities (e.g., see Kuijken et al. 2015; de Jong et al. 2017). The combined set of the 440 survey tiles of DR3 mostly comprises a small number of large contiguous areas, see Fig. 1. This enables a refinement of the photometric calibration that exploits both the overlap between observations within a filter as well as the stellar colours across filters (de Jong et al. 2017).<sup>1</sup>

<sup>1</sup> The data products that constitute the main DR3 release (stacked images, weight and flag maps, and single-band source lists for 292 survey tiles, as well as a multi-band catalogue for the combined DR1, DR2 and DR3 survey area of 440 survey tiles), are released via the ESO Science Archive, and they are also accessible via the Astro-WISE system

### 2.1. Galaxy catalogue

The KiDS galaxy catalogue provides the spatial coordinates, the 2 arcsec aperture photometry in four bands ( $u, g, r, i$ ) and photometric redshifts for all galaxies down to the  $5\sigma$  limiting magnitudes of 24.3, 25.1, 24.9 and 23.8 in the four bands, respectively. We chose to avoid the use of galaxy colours to detect clusters in order to minimise the dependence of the selection function on the presence (or absence) of the red-sequence of cluster galaxies (Maturi et al. 2019). For more information about the shear and redshift properties of the entire galaxy catalogue see de Jong et al. (2017) and Hildebrandt et al. (2017).

#### 2.1.1. Galaxy shape measurements

The original shear analysis of the KiDS-DR3 data has been described in Kuijken et al. (2015) and Hildebrandt et al. (2017). The shape measurements has been performed with *lensfit* (Miller et al. 2007, 2013) and successfully calibrated for the KiDS-DR3 data in Fenech Conti et al. (2017).

In this work, the data used for shape measurements are those in the  $r$ -band, being the ones with the best seeing properties and with highest source density. The error on the multiplicative shear calibration, estimated from simulations with *lensfit* and benefiting from a self-calibration, is of the order of 1% (Hildebrandt et al. 2017). The final catalogue KiDS-DR3 gives shear measurements for  $\sim 15$  million of galaxies, with an effective number density of  $n_{\text{eff}} = 8.53 \text{ galaxies arcmin}^{-2}$  (as defined in Heymans et al. 2012), over a total effective area of  $360 \text{ deg}^2$ .

#### 2.1.2. Galaxies photometric redshifts

The original properties of photometric redshifts (photo- $z$ ) of KiDS galaxies are described in Kuijken et al. (2015) and de Jong et al. (2017). The photo- $z$ s were extracted with BPZ (Benítez 2000; Hildebrandt et al. 2012), a Bayesian photo- $z$  estimator based upon template fitting, from the 4-band ( $u, g, r, i$ ). Furthermore, BPZ returns a photo- $z$  posterior probability distribution function which AMICO fully exploits. When compared with spectroscopic redshifts from the Galaxy And Mass Assembly (GAMA, Liske et al. 2015) spectroscopic survey of low redshift galaxies, the resultant accuracy is  $\sigma_z \sim 0.04(1+z)$ , as shown in de Jong et al. (2017).

### 2.2. Cluster catalogue

As already mentioned, the galaxy cluster catalogue we use in this work has been extracted from KiDS-DR3 using the AMICO algorithm. In particular, we analyse the same cluster catalogue adopted by Bellagamba et al. (2019). Its full description and validation can be found in Maturi et al. (2019). Here, we present the main properties of this cluster catalogue. Let us premise that the cluster detection through AMICO on KiDS-DR3 is an enhancement of the work by Radovich et al. (2017) on DR2, both in terms of total covered area ( $438 \text{ deg}^2$  against  $114 \text{ deg}^2$ ) and of detection algorithm with respect to the previous matched filter method (Bellagamba et al. 2011). From the initial covered  $438 \text{ deg}^2$ , all clusters belonging to those regions heavily affected by satellite tracks, haloes created by bright stars, and image artefacts are rejected (Maturi et al. 2019). Furthermore, we select

([http://kids.strw.leidenuniv.nl/DR1/access\\_aw.php](http://kids.strw.leidenuniv.nl/DR1/access_aw.php)) and the KiDS website <http://kids.strw.leidenuniv.nl/DR3>.

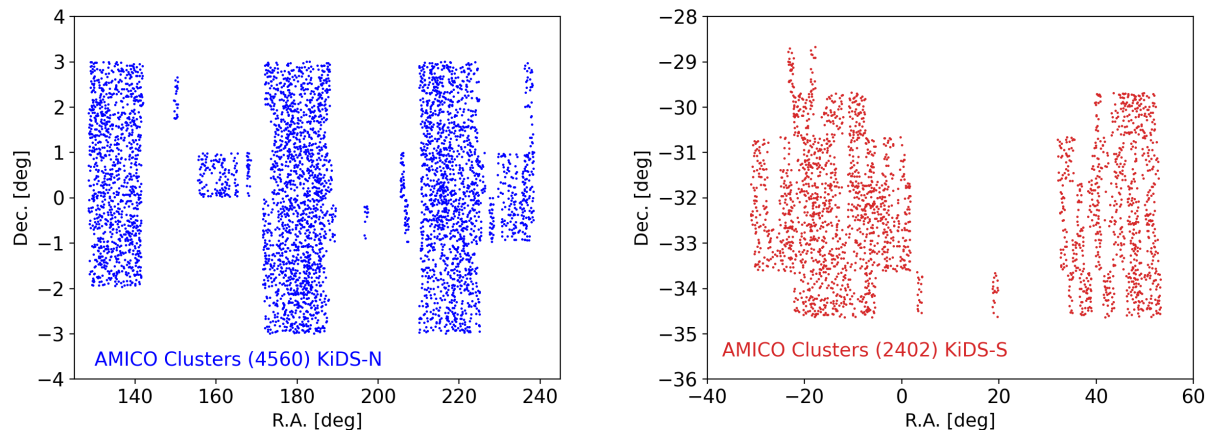


**Fig. 1.** Distribution of cluster centres in angular coordinates of the 6962 detections by AMICO divided in the KiDS-N (left) and KiDS-S (right) areas. Systems with  $0.1 \leq z \leq 0.6$  and with  $S/N > 3.5$  are displayed.

only detections with  $S/N > 3.5$ <sup>2</sup>. Finally, we narrowed the redshift range to  $0.1 \leq z \leq 0.6$ , for a final sample of 6962 galaxy clusters. Objects at  $z < 0.1$  are discarded because of their low lensing power, while those at  $z > 0.6$  are excluded because the background galaxies density in KiDS data is too small to allow a robust weak lensing analysis. Furthermore, collecting clusters with  $0.1 \leq z \leq 0.6$  we can robustly separate the clustered objects from the population of background galaxies. For each cluster we select galaxy population, excluding the galaxies whose most likely redshift  $z_s$  is not significantly higher than the lens one  $z_l$ :

$$z_{s,min} > z_l + \Delta z, \quad (1)$$

where  $z_{s,min}$  is the lower bound of the region including the  $2\sigma$  of the probability density distribution and  $\Delta z$  is set to 0.05, similar to the typical uncertainty on photometric redshifts in the galaxy catalogue and well larger than the uncertainty on the cluster redshifts.

The criterion based on the photometric redshift distribution aims at keeping only galaxies which have a well-behaved redshift probability distribution and have a negligible probability of being at redshift equal to or lower than the cluster. In addition we consider the flag ODD to be larger than 0.8 and  $0.2 \leq z_s \leq 1$ .

Left and right panel of Fig. 1 display the angular distribution of galaxy clusters detected by AMICO in the (R.A., Dec) coordinate system in the KiDS-N and KiDS-S sky area covered by the DR3 data, respectively. We use the masks from the two sky areas to generate random samples of positions, which are needed to construct tangential shear profiles around random points (see the discussion on systematics in Section 4).

AMICO searches for cluster candidates by convolving the 3D galaxy distribution with a redshift-dependent filter, defined as the ratio between a cluster signal and a noise model. Such a convolution is able to create a 3D amplitude map, where every peak constitutes a possible detection. Then, for each cluster candidate, AMICO returns angular positions, redshift,  $S/N$  and the signal amplitude  $A$ , which is a measure of the cluster galaxy abundance.

<sup>2</sup> The method used to assess the quality of the detections exploits realistic mock catalogues constructed from the real data themselves, as described in Section 6.1 of Maturi et al. (2019). These mock catalogues are used to estimate the uncertainties on the quantities characterising the detections, as well as the purity and completeness of the entire sample.

In Bellagamba et al. (2018) it has been demonstrated, using simulations, that the amplitude is a well-behaved mass-proxy, provided that the model calibration is accurate enough. The signal amplitude is defined as:

$$A(\theta_c, z_c) \equiv \alpha^{-1}(z_c) \sum_{i=1}^{N_{gal}} \frac{M_c(\theta_i - \theta_c, m_i) p_i(z_c)}{N(m_i, z_c)} - B(z_c), \quad (2)$$

where  $\theta_c$  are the cluster sky coordinates,  $M_c$  is the cluster model (i.e the expected density of galaxies per unit magnitude and solid angle) at the cluster redshift  $z_c$ ,  $N$  the noise distribution,  $p_i(z)$ ,  $\theta_i$  and  $m_i$  indicate the photometric redshift distribution, the sky coordinates and the magnitude of the  $i$ -th galaxy, respectively; the parameters  $\alpha$  and  $B$  are redshift dependent functions providing the normalisation and the background subtraction, respectively.

The cluster model  $M_c$  is described by a luminosity function and a radial density profile, obeying to the formalism presented in Bellagamba et al. (2018); derived from the observed galaxy population of clusters detected through the SZ-effect (Hennig et al. 2017), as described in detail in Maturi et al. (2019). Furthermore, AMICO assigns to each galaxy in a sky region a probability to be part of a given detection, defined as:

$$P(i \in j) \equiv P_{f,i} \frac{A_j M_{c,j}(\theta_i - \theta_j, m_i) p_i(z_j)}{A_j M_{c,j}(\theta_i - \theta_j, m_i) p_i(z_j) + N(m_i, z_j)}, \quad (3)$$

where  $A_j$ ,  $\theta_j$  and  $z_j$  are the amplitude, the sky coordinates and the redshift of the  $j$ -th detection, respectively.  $P_{f,i}$  is the field probability of the  $i$ -th galaxy before the  $j$ -th detection is defined. Indeed, in this application to KiDS-DR3 data, the adopted filter includes galaxy coordinates,  $r$ -band magnitudes and the full photometric redshift distribution  $p(z)$ .

The distributions in redshift and amplitude of this sample are shown in Bellagamba et al. (2019). In the following analysis we will divide the sample in three redshift bins:

- $0.1 \leq z < 0.3$ ,
- $0.3 \leq z < 0.45$ ,
- $0.45 \leq z \leq 0.6$ .

Those bins have been chosen with aim of having almost the same number of clusters and numerous enough also to study the amplitude trends, in each of them.

### 2.3. Measuring the tangential shear profile

Using the tangential component of the shear signal  $\gamma_t$  we can write the excess surface mass density as:

$$\Delta\Sigma(r) = \bar{\Sigma}(< r) - \Sigma(r) \equiv \Sigma_{\text{crit}}\gamma_t, \quad (4)$$

where  $\Sigma(r)$  represents the mass surface density of the lens at distance  $r$  and  $\bar{\Sigma}(< r)$  its mean within  $r$ ;  $\Sigma_{\text{crit}}$  indicates the critical surface density (Bartelmann & Schneider 2001) that can be read as:

$$\Sigma_{\text{crit}} = \frac{c^2}{4\pi G} \frac{D_l}{D_s D_{ls}}, \quad (5)$$

with  $D_l$ ,  $D_s$  and  $D_{ls}$  are the angular diameter distances observer-lens, observer-source and source-lens, respectively;  $c$  represents the speed of light and  $G$  the universal gravitational constant.

Selecting all background sources of each cluster-lens, as underlined before in the text, we can compute the tangential component of the shear with respect to the cluster centre  $\gamma_t$ . This allow us to construct the excess surface mass density profile at distance  $r_j$  from the following relation:

$$\Delta\Sigma(r_j) = \left( \frac{\sum_{i \in j} (w_i \Sigma_{\text{crit},i}^{-2}) \gamma_{t,i} \Sigma_{\text{crit},i}}{\sum_{i \in j} (w_i \Sigma_{\text{crit},i}^{-2})} \right) \frac{1}{1 + K(r_j)} \quad (6)$$

where  $w_i$  indicates the weight assigned to the measurement of the source ellipticity and  $K(r_j)$  the average correction due to the multiplicative noise bias in the shear estimate as in Eq. (7) by Bellagamba et al. (2019). To compute the critical surface density for the  $i$ -th galaxy we use the most probable source redshift as given by BPZ.

When stacking the excess surface mass density profile of clusters in equal amplitude and redshift bin we refer to the following relation:

$$\Delta\Sigma_N(r_j) = \frac{\sum_{n \in N} W_{n,j} \Delta\Sigma_n(r_j)}{\sum_{n \in N} W_{n,j}}, \quad (7)$$

where  $N$  represents the bin in which we perform the stacking and  $W_{n,j}$  indicates the weight for the  $j$ -th radial bin of the  $n$ -th cluster:

$$W_{n,j} = \sum_{i \in j} w_i \Sigma_{\text{crit},i}^2. \quad (8)$$

## 3. Models

We model the stacked lensing signal with the projected halo model formalism. The total density profile is constructed considering the signal coming from the central part of the cluster, called the 1-halo term, and the one caused by correlated large-scale structures, called the 2-halo term.

### 3.1. The 1-halo lens model

The radial density profile of the cluster main halo is modelled considering a smoothly-truncated Navarro-Frenk-White (NFW, Navarro et al. 1997) density profile (Baltz et al. 2009):

$$\rho(r) = \frac{\rho_s}{(r/r_s)(1+r/r_s)^2} \left( \frac{r_t^2}{r^2 + r_t^2} \right)^2, \quad (9)$$

where  $\rho_s$  represents the typical matter density within the scale radius  $r_s$ , and  $r_t$  indicates the truncation radius, typically expressed in terms of the halo radius  $R_{200}$  - the radius enclosing

200 times the critical density of the Universe at the considered redshift  $\rho_c(z)$ :  $r_t = t R_{200}$  with  $t$  the truncation factor. The scale radius is commonly parametrised as  $r_s = R_{200}/c_{200}$ , where  $c_{200}$  represents the concentration parameter, which is correlated with the halo mass and redshift depending on the halo mass accretion history (Macciò et al. 2007; Neto et al. 2007; Macciò et al. 2008; Zhao et al. 2009; Giocoli et al. 2012b). The total mass enclosed within the radius  $R_{200}$ ,  $M_{200}$ , can be seen as the normalisation of the model and a mass-proxy of the true enclosed mass of the dark matter halo hosting the cluster (Giocoli et al. 2012a).

This truncated version of the NFW model was deeply tested in simulations by Oguri & Hamana (2011), demonstrating that it describes the cluster profiles more accurately than the original NFW profile model, up to about 10 times the radius enclosing 200 times the critical density of the Universe. In fact, one of the main advantages of the truncation radius is that it removes the non-physical divergence of the total mass at large radii. Moreover, the Baltz et al. (2009) model describes accurately the transition between the cluster main halo and the 2-halo contribute (Cacciato et al. 2009; Giocoli et al. 2010; Cacciato et al. 2012), providing less biased estimates of mass and concentration from shear profiles (Serenio et al. 2017). Neglecting the truncation, the mass would be underestimated and the concentration overestimated. As we are considering only stacked shear profiles, the NFW model provides a reliable description even though it is based on the assumption of spherical symmetry. In fact, when stacking several shear profiles, the intrinsic halo triaxiality tends to assume a spherical radial symmetry on the stacked profile, for statistical reasons. This is the reason why the weak lensing cross-correlation provides a direct estimate of the mean mass for clusters in a given range of observable properties. As reference model, we set  $r_t = 3$  for every amplitude and redshift bins, as done e.g. by Bellagamba et al. (2019), following the results by Oguri & Hamana (2011). However, we will discuss how the mass and concentration estimates change when assuming different values of the truncation radius.

When analysing the weak lensing by clusters, an important source of bias is the inaccurate identification of the lens centre. In this study, we assume those determined by AMICO in the detection procedure. However, the detection is performed through a grid which induces an intrinsic uncertainty due to the pixel size, that is  $< 0.1$  Mpc/h (Bellagamba et al. 2018). Furthermore, it must be taken into account that the galaxy distribution centre may appreciably deviate from the mass centre of the system - or the location of the minimum potential, especially for unrelaxed systems with ongoing merging events. For example, in Johnston et al. (2007) it was found that the Brightest Central Galaxy (BCG), defining the cluster centre, might be misidentified and, in that case, the value of  $\Delta\Sigma$  at small scales is underestimated, biasing low the measurement of the concentration by  $\sim 15\%$  and consequently underestimating the mass by  $\sim 10\%$ . Moreover, George et al. (2012) found that the halo mass estimates from stacked weak lensing can be biased low by 5%-30%, if inaccurate centres are considered and the issue of off-centring is not addressed.

In our procedure we will account for this effect by considering a second additional component in our model, which is the one produced by haloes whose observed centres have a non-negligible deviation with respect to the centres assumed by the stacking procedure, as provided by the AMICO cluster finder. In doing so we follow the method adopted by Johnston et al. (2007) and Viola et al. (2015). First, we define the rms of the misplacement of the haloes,  $\sigma_{\text{off}}$ , assuming an azimuthally symmetric Gaussian distribution. Thereby, the probability of a lens being

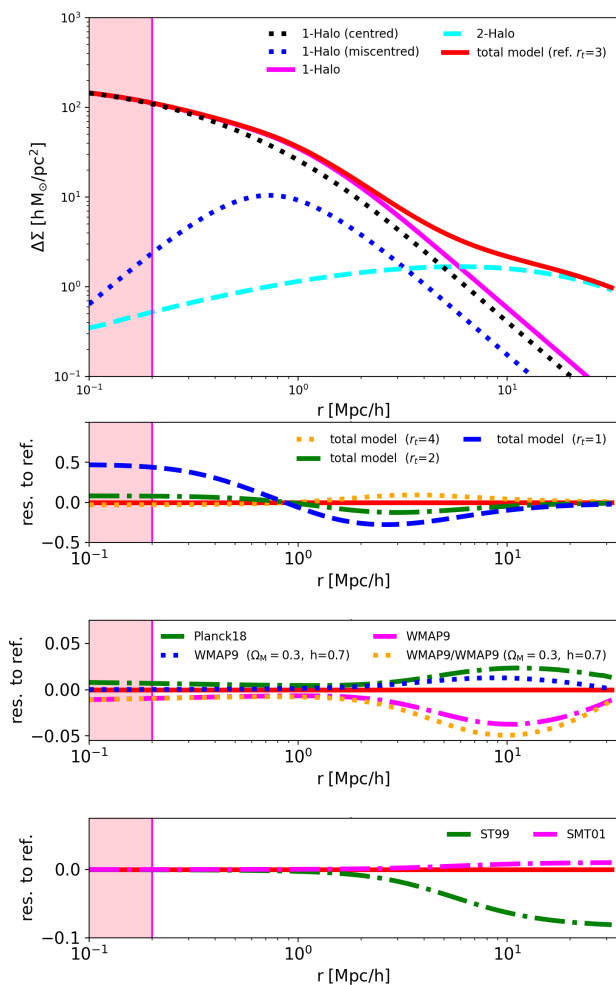


**Fig. 2.** *Upper panel:* model of the projected excess of surface mass density, as a function of the comoving radial distance from the centre, for a cluster with  $M_{200} = 10^{14} M_{\odot}/h$ ,  $c_{200} = 3$  at redshift  $z = 0.3$ , with  $\sigma_{\text{off}} = 0.3$  and  $f_{\text{off}} = 0.3$ . The radius enclosing 200 times the critical density corresponds to  $R_{200} = 1.47$  Mpc/h. The four 1-halo and 2-halo terms are shown with different colours and styles, as reported in the labels. *Second panel:* the relative differences, with respect to the reference, of the models with  $r_t = 1, 2$  and 4. *Third panel:* the relative differences, with respect to the reference, of the models with the linear power spectrum estimated assuming different cosmological model parameters, as reported in the labels. For comparison, we display with yellow dotted curve the relative difference between the prediction adopting WMAP9 cosmology and WMAP9 but fixing  $\Omega_M = 0.3$  and  $h = 0.7$ . *Bottom panel:* the relative differences, with respect to the reference, of two models constructed with either the Sheth & Tormen (1999) or the Tinker et al. (2010) biasing model.

at distance  $R_s$  from the assumed centre, or briefly the probability distribution of the offsets, can be defined as:

$$P(R_s) = \frac{R_s}{\sigma_{\text{off}}} \exp\left[-\frac{1}{2}\left(\frac{R_s}{\sigma_{\text{off}}}\right)^2\right], \quad (10)$$

where  $\sigma_{\text{off}}$  represent the scale length, whose typical values found e.g. by SDSS collaboration can be of the order of  $\sigma_{\text{off}} \sim 0.4$  Mpc/h (Johnston et al. 2007). While modelling the halo profile, we will assume that a fraction  $f_{\text{off}}$  of the lenses is miscentred. Now, we can introduce the azimuthally averaged profile of a population misplaced by a distance  $R_s$  in the lens plane (Yang et al.

2006):

$$\Sigma(R|R_s) = \frac{1}{2\pi} \int_0^{2\pi} \Sigma_{\text{cen}}(R) \left( \sqrt{R^2 + R_s^2 + 2RR_s \cos\theta} \right) d\theta, \quad (11)$$

where  $\Sigma_{\text{cen}}(R)$  refers to the centred surface brightness distribution (or briefly the centred profile) derived by integrating  $\rho(r)$  along the line-of-sight. Finally, integrating Eq. (11) along  $R_s$  and weighing each offset distance according to Eq. (10), we can obtain the mean surface density distribution of a miscentred halo population:

$$\Sigma_{\text{off}}(R) = \int P(R_s) \Sigma(R|R_s) dR_s. \quad (12)$$

Our final model for the 1-halo term can be written as the sum of a centred an off-centred population:

$$\Sigma_{1h}(R) = (1 - f_{\text{off}}) \Sigma_{\text{cen}}(R) + f_{\text{off}} \Sigma_{\text{off}}(R). \quad (13)$$

Generally, this 1-halo model depends on nine parameters but, when analysing the 1-halo radial range only data-set – where the large scale contribution is almost negligible, we fix the cosmology to a flat  $\Lambda$ -CDM with  $h = 0.7$ ,  $\Omega_M = 0.3$  and  $\Omega_{\Lambda} = 0.7$ , the truncation factor to the reference value  $r_t = 3$  and the effective redshift estimated by the weight of the stacked samples in each bin. Therefore our analysis on the 1-halo radial range uses a model that depends on four free parameters:  $M_{200}$ ,  $c_{200}$ ,  $\sigma_{\text{off}}$  and  $f_{\text{off}}$ . We underline that analysing the data-set up to large scales to constrain the total matter density parameter, we accordingly re-scale both the data and the models to the new cosmology.

In our analysis we will neglect the measurements below 0.2 Mpc/h mainly for three reasons. Firstly, from an observational point of view, the uncertainties in the measure of photo- $z$ s and shear close to the cluster centre are large because of the contamination due to the higher concentration of cluster galaxies. Secondly, the shear signal analysis in close proximity to the cluster centre is sensitive to the BCG contribution to the matter distribution, and to deviations from the weak lensing approximation used in the profile model. Lastly, this choice mitigates the miscentring effects. Thus, neglecting small-scale measurements minimises the systematics possibly affecting the estimation of the concentration  $c_{200}$ , which would otherwise be overestimated - being degenerate with the  $\sigma_{\text{off}}$  and  $f_{\text{off}}$  parameters.

### 3.2. The 2-halo lens model

Here we introduce the 2-halo model used to describe the surface density profiles beyond the cluster radius. The data for  $r > R_{200}$  can be used to constrain the cosmological parameters. In particular, we will focus on the total matter density,  $\Omega_M$ .

At scales larger than the radius  $R_{200}$ , the shear signal is caused by the correlated matter distribution around the galaxy clusters and it manifests as an increase of the mass density profiles. In practice, the 2-halo term characterises the cumulative effects of the large-scale structures in which galaxy clusters are located. The uncorrelated matter distribution along the line-of-sight does produce only a modest contribution to the stacked shear signal. We will model the 2-halo term following the recipe by Oguri & Takada (2011).

It is worth noticing that the 2-halo term contribution at small radii is expected to be negligible, becoming statistically significant only at scales  $\gtrsim 5$  Mpc/h. The total excess surface mass density profile will be the sum of the halo profile described by

the Eq. (13) with the contribution due to the matter in correlated haloes that we can write as (Oguri & Takada 2011; Oguri & Hamana 2011; Sereno et al. 2017):

$$\Delta\Sigma_{2h}(\theta; M_{200}, z) = \int \frac{ldl}{2\pi} J_2(l\theta) \frac{\bar{\rho}_m(z)b_h(M_{200}; z)}{(1+z)^3 D_l^2(z)} P_{lin,m}(k_l; z), \quad (14)$$

where  $z$  represents the cluster redshift, estimated using photometric data, as provided by AMICO. The other terms in Eq. (14) are summarised as follows:

- $\theta$  is the angular scale. It is computed as the ratio between the projected radius, at which the shear signal is measured, and the corresponding lens angular diameter distance  $D_l(z)$  [Mpc/h], evaluated at the cluster redshift and assuming a flat  $\Lambda$ CDM cosmology.
- $J_2$  is the Bessel function of second type, which is the solution of the Bessel differential equation, with a singularity at the origin. This is a function of  $l\theta$ , where  $l$  is the integration variable and the momentum of the wave vector  $k_l$  for the linear power spectrum of matter fluctuations  $P_{lin,m}$ .
- $k_l = l/(1+z)D_l(z)$  indicates the wave vector module.
- $\bar{\rho}_m(z)$  represents the mean cosmic background density at the lens redshift, in unit of  $M_\odot \text{Mpc}^{-3} h^2$ .
- $P_{lin,m}(k_l; z)$  is the linear power spectrum of matter computed according to the Eisenstein & Hu (1999) transfer function. For our reference case, when computing the linear matter power spectrum we adopt the Planck18 (Planck Collaboration et al. 2020) cosmological parameters though fixing  $\Omega_M = 0.3$ ,  $\Omega_\Lambda = 0.7$  and  $h = 0.7$ . The adopted Eisenstein & Hu (1999) transfer function model is accurate enough given our current measurement uncertainties. We tested the method using the CAMB model (Lewis et al. 2000), finding negligible differences.
- $b_h(M; z)$  indicates the halo bias, for which we adopt the Tinker et al. (2010) model, that has been successfully tested and calibrated using a large data-set of numerical simulations. In our work we will also test the robustness, and eventual biases, of our results using the bias models by Sheth & Tormen (1999) and Sheth et al. (2001). The halo bias is expected to be constant at large scales and to evolve weakly with redshift. It is expressed as (the square root of) the ratio between the halo and the linear dark matter power spectra. At fixed redshift the bias amplitude increases with the halo mass. However, it is typically parametrised in terms of the peak-high of the matter density field: highest peaks - which represent the seeds from which galaxy clusters form - tend to be more biased than the smallest ones (Mo & White 1996).

### 3.3. The full lens model

The full model of the projected excess of surface mass density adopted in this work can be read as:

$$\Delta\Sigma_{model}(R) = \Delta\Sigma_{1h}(R) + \Delta\Sigma_{2h}(R), \quad (15)$$

where  $\Delta\Sigma_{1h}$  and  $\Delta\Sigma_{2h}$  are computed with Eqs. (13) and (14), respectively.

Figure 2 (upper panel) shows the different components of the adopted lens model given by Eq. (15) for the reference case of a halo with mass  $M_{200} = 10^{14} M_\odot/h$ ,  $c_{200} = 3$  at redshift  $z_l = 0.3$ , with  $\sigma_{off} = 0.3$  and  $f_{off} = 0.3$ . The effect of the truncation radius is shown in the second panel, where we report the relative differences, with respect to the reference model, of the cases with  $r_t = 1, 2$  and 4. In projection, we can notice that the impact of the

truncation radius not only modifies matter density distribution at scales larger than 1 Mpc/h but also reshapes the matter density distribution on small scales to preserve the matter enclosed within  $R_{200}$ . The impact of assuming a different cosmological model when computing the linear matter power spectrum is displayed in the third panel. Particularly, the yellow dotted curve displays the ratio between the prediction assuming the WMAP9 cosmological model and those adopting  $\Omega_M = 0.3$  and  $h = 0.7$ , fixing the other parameters to the flat WMAP9 case. The green and magenta dot-dashed and the blue dotted curves display the relative difference of the Planck18, WMAP9 and WMAP9 with  $\Omega_M = 0.3$  and  $h = 0.7$  with respect to our reference model (we assume Planck18 cosmological parameters but setting  $\Omega_M = 0.3$  and  $h = 0.7$ ), respectively. Finally, in the bottom panel we exhibit the relative difference between the reference model, where we assume the Tinker et al. (2010) halo bias, and two alternative models constructed assuming either the Sheth & Tormen (1999) biasing model or the Sheth et al. (2001) one. The halo bias model mainly affects the  $\Delta\Sigma$  profile toward large scales. We also notice that, for this cluster mass and redshift, the Sheth et al. (2001) model is slightly above our reference one, while the Sheth & Tormen (1999) case starts to decrease already at 1 Mpc/h reaching almost 10% difference at scales larger than 10 Mpc/h. In Appendix B we test the impact of different bias model assumption in the estimate of the total matter density parameter.

## 4. Results

In this section we present the main results of our analysis. Firstly, we will model the small-scale stacked surface mass density profiles, assessing the structural properties of the hosting halo population. Then we will model the full lensing signal up to the largest available scales, constraining the total matter density parameter,  $\Omega_M$ .

In the first part of our analysis, when modelling the small-scale signal coming from the central part of the clusters only, we will limit to scales between 0.2 and 3.16 Mpc/h. We refer to this analysis as the  $\sim 1h$ -case, since most of the contribution to the measured signal comes from the main dark matter haloes hosting the galaxy clusters. In fact, as evident from the upper panel of Figure 2, the 2-halo term affects, to a small degree, only the few last radial bins available. This makes our inference on the cluster halo structural properties, expressed in terms of the four 1-halo (NFW) model parameters ( $M_{200}$ ,  $c_{200}$ ,  $f_{off}$  and  $\sigma_{off}$ ), much less dependent on the uncertain details of the halo biasing model. To test this assumption, we repeated the following analysis including only the 1-halo contribution, finding that the mass is slightly overestimated by few percents (see Tab. 1 for more details). For each corresponding case, in parenthesis we report the  $\chi^2$  divided by the number of degrees of freedom. We recall that the highest  $S/N$  comes from small-scale lensing in this kind of measures, but it may be affected by both theoretical and observational systematic uncertainties (Mandelbaum et al. 2013).

Subsequently, we will model the total stacked density profiles up to 35 Mpc/h. In this case, we will consider Gaussian priors on the four parameters of the 1-halo term, with the mean and the standard deviation corresponding to the posterior distribution results. The main goal here is to derive constraints on  $\Omega_M$  marginalised over the 1-halo term parameters. We will refer to this cosmological analysis as the  $1h + 2h$ -case.

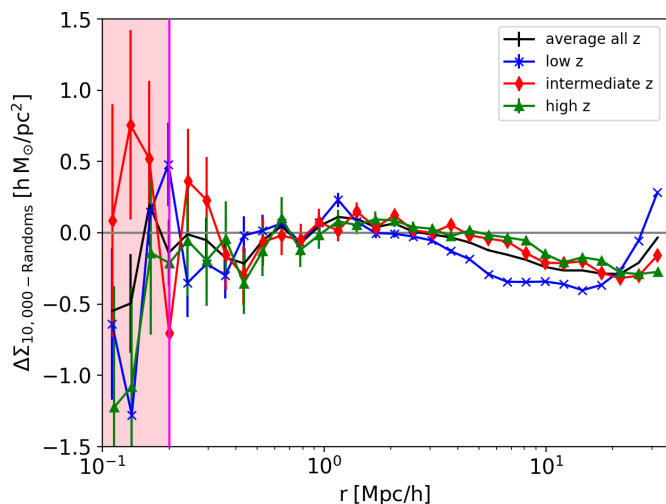


**Fig. 3.** Excess of surface mass density profile around random centres for the three redshift bins in which the AMICO clusters have been divided: low ( $0.1 \leq z < 0.3$ ), intermediate ( $0.3 \leq z < 0.45$ ) and high ( $0.45 \leq z \leq 0.6$ ) redshift. We have created 10,000 realisations of the sample using random centres. The blue crosses, red diamonds and green triangles show the average measurements in the three redshift intervals - extending the profiles up to 35 Mpc/h as in the  $1h + 2h$ -case. The black line display the average over all redshifts. The error bars show square-root of the diagonal terms of the corresponding covariances  $C_{\text{Randoms}}(r, r')$ . The vertical pink area on the left part of the figure marks the data points below 0.2 Mpc/h that we will not consider in our analysis.

#### 4.1. Constraining the cluster structural properties

In this Section we model the stacked shear profiles collected in the  $0.2 < R < 3.16$  Mpc/h radial range, while in the next one we will exploit the profiles measured up to 35 Mpc/h – where the 2-halo term contribute dominantes. In both cases we bin the dataset adopting a logarithmic binning along the radial directions, choosing a  $d \log(r) \approx 0.1$  we have 14 and 30 radial bins for the two cases,  $\sim 1h$  and  $1h + 2h$ , respectively. In both cases the analyses are based on a set of 14 stacked excess surface density profiles of clusters, obtained by dividing the whole AMICO-KiDS-DR3 cluster catalogue in redshift and amplitude, as reported in the first four columns of Tab. 1.

In order to properly model the large-scale weak lensing signal we need to take into account most of the systematics and uncertainties that could emerge in the very weak regime where the excess surface mass density becomes low. We perform this by constructing stacked profiles around random positions in different redshift bins, that we subtract to the stacked cluster profiles (Sereno et al. 2018; Bellagamba et al. 2019). We generate 10,000 realisations of a sample of 6962 random positions properly accounting for the KiDS-DR3 survey masks (Fig. 1) and the cluster redshift distribution. The number of random realisations has been selected finding a good compromise between the computational cost needed for the analyses and number of AMICO clusters used in this work. In Fig. 3 we display the excess surface mass density profiles around the random centres for the three different redshift range considered, as well as the average one (for simplicity we exhibit only the data-set for the  $1h + 2h$ -case). The error bars are the square-root of the diagonal terms of the corresponding covariances  $C_{\text{Randoms}}(r, r')$  computed constructing the excess surface mass density around random centres:

$$C_{\text{Randoms}}(r, r') = \langle (\Delta\Sigma(r) - \bar{\Delta\Sigma}(r)) (\Delta\Sigma(r') - \bar{\Delta\Sigma}(r')) \rangle \quad (16)$$

**Table 1.** AMICO cluster sample binned in redshift and amplitude as used in our analyses. The table reproduces the structure adopted by Bellagamba et al. (2019); we report in the  $\log M_{200}$  columns the values we obtain modelling the two cases:  $\sim 1h$  (up to 3.16 Mpc/h) and  $1h + 2h$  (up to 35 Mpc/h). The numbers, expressed in  $\log(M_{200}/h^{-1} M_{\odot})$ , reported refer to the median and the  $18th - 82nd$  percentile widths. The values reported in parenthesis represent the number of *d.o.f.* corresponding to each considered case. The column  $N_{cl}$  expresses the number of clusters stacked in each bin.

	$z$ range	$z_{\text{eff}}$	A range	$A_{\text{eff}}$	$\log M_{200}: \sim 1h$ , with $1h$ mod.	$\log M_{200}: \sim 1h$ with $1h + 2h$ mod.	$\log M_{200}: 1h + 2h$	$N_{cl}$
1	[0.10, 0.30]	$0.190 \pm 0.002$	[0, 1]	$0.830 \pm 0.003$	$13.208^{+0.078}_{-0.083}$ (1.877)	$13.170^{+0.079}_{-0.078}$ (1.827)	$13.198^{+0.059}_{-0.061}$ (0.955)	1066
2	[0.10, 0.30]	$0.207 \pm 0.002$	[1, 1.55]	$1.213 \pm 0.006$	$13.550^{+0.071}_{-0.074}$ (2.905)	$13.514^{+0.071}_{-0.064}$ (1.670)	$13.504^{+0.052}_{-0.051}$ (0.983)	822
3	[0.10, 0.30]	$0.212 \pm 0.004$	[1.55, 2.05]	$1.762 \pm 0.010$	$14.059^{+0.054}_{-0.058}$ (1.191)	$14.035^{+0.054}_{-0.057}$ (0.933)	$14.009^{+0.048}_{-0.051}$ (1.134)	240
4	[0.10, 0.30]	$0.226 \pm 0.005$	[2.05, 2.75]	$2.350 \pm 0.021$	$14.239^{+0.061}_{-0.056}$ (0.648)	$14.215^{+0.061}_{-0.056}$ (0.450)	$14.209^{+0.053}_{-0.059}$ (0.851)	96
5	[0.10, 0.30]	$0.211 \pm 0.008$	[2.75, 6.5]	$3.259 \pm 0.084$	$14.532^{+0.059}_{-0.074}$ (2.441)	$14.510^{+0.056}_{-0.062}$ (1.747)	$14.567^{+0.050}_{-0.059}$ (1.122)	41
6	[0.30, 0.45]	$0.378 \pm 0.001$	[0, 1.15]	$0.954 \pm 0.004$	$13.607^{+0.063}_{-0.073}$ (1.846)	$13.576^{+0.062}_{-0.067}$ (1.500)	$13.593^{+0.051}_{-0.049}$ (1.560)	1090
7	[0.30, 0.45]	$0.382 \pm 0.002$	[1.15, 1.65]	$1.354 \pm 0.006$	$13.870^{+0.069}_{-0.073}$ (1.322)	$13.836^{+0.067}_{-0.068}$ (0.566)	$13.860^{+0.056}_{-0.057}$ (0.596)	762
8	[0.30, 0.45]	$0.385 \pm 0.002$	[1.65, 2.3]	$1.909 \pm 0.012$	$14.208^{+0.055}_{-0.057}$ (1.497)	$14.175^{+0.054}_{-0.057}$ (0.953)	$14.224^{+0.036}_{-0.038}$ (0.678)	339
9	[0.30, 0.45]	$0.392 \pm 0.004$	[2.3, 3]	$2.585 \pm 0.022$	$14.280^{+0.078}_{-0.077}$ (1.518)	$14.256^{+0.074}_{-0.076}$ (1.023)	$14.229^{+0.063}_{-0.067}$ (1.551)	98
10	[0.30, 0.45]	$0.377 \pm 0.007$	[3, 6.5]	$3.577 \pm 0.071$	$14.588^{+0.065}_{-0.073}$ (2.697)	$14.560^{+0.064}_{-0.074}$ (1.818)	$14.512^{+0.062}_{-0.055}$ (0.911)	43
11	[0.45, 0.60]	$0.496 \pm 0.001$	[0, 1.3]	$1.108 \pm 0.004$	$13.707^{+0.082}_{-0.084}$ (1.271)	$13.669^{+0.074}_{-0.085}$ (1.008)	$13.682^{+0.068}_{-0.068}$ (1.387)	984
12	[0.45, 0.60]	$0.516 \pm 0.002$	[1.3, 1.8]	$1.516 \pm 0.005$	$13.877^{+0.071}_{-0.074}$ (1.586)	$13.838^{+0.065}_{-0.069}$ (1.373)	$13.848^{+0.058}_{-0.056}$ (1.181)	889
13	[0.45, 0.60]	$0.515 \pm 0.003$	[1.8, 2.5]	$2.071 \pm 0.011$	$14.180^{+0.075}_{-0.076}$ (3.897)	$14.145^{+0.074}_{-0.074}$ (3.496)	$14.112^{+0.069}_{-0.069}$ (1.951)	373
14	[0.45, 0.60]	$0.510 \pm 0.004$	[2.5, 6.5]	$2.877 \pm 0.039$	$14.377^{+0.076}_{-0.080}$ (1.914)	$14.350^{+0.076}_{-0.079}$ (1.556)	$14.314^{+0.069}_{-0.068}$ (1.400)	119

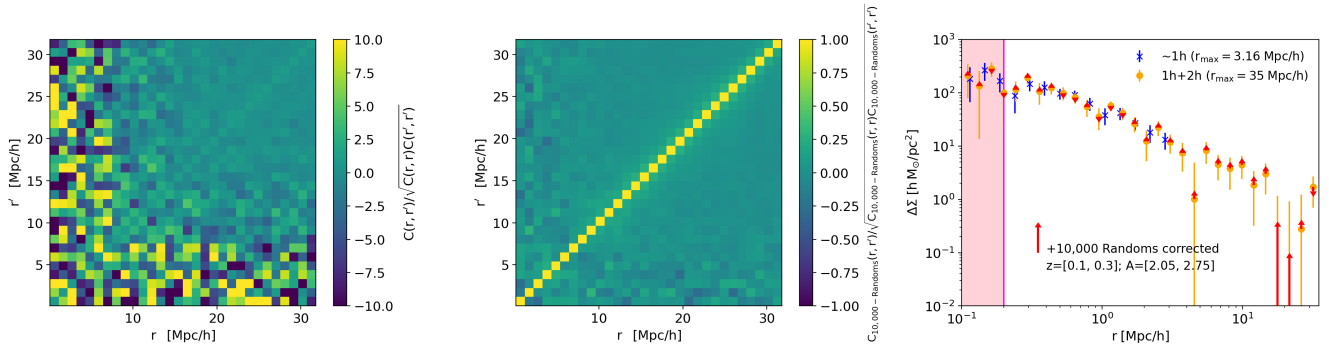


**Fig. 4.** *Left panel:* the normalised covariance of the data-set corresponding to the bin with  $0.1 \leq z < 0.3$  and  $2.05 \leq A < 2.75$ , stacking 96 detected clusters, computed with 10,000 bootstrap realisations of the stacked profile. *Central panel:* the normalised covariance of the 10,000 realisations of the whole AMICO sample, randomly distributed in the survey footprints. *Right panel:* the stacked excess surface mass density profile of the  $1h$ -case (blue crosses) and  $1h + 2h$ -case (orange circles). In both cases we subtract to the data points the stacked profiles around random centre. The error bars refer to the square-root of the diagonal elements of the final covariance (Eq. 17). The red arrows indicate the variation of the stacked profile when, for the corresponding redshift bin, the random contributions are subtracted from the data.

where  $\bar{\Delta\Sigma}(r)$  indicates the average profile over the considered random data-set. All the average profiles are consistent with zero, showing only a mild deviation at large distances, due to the survey masks.

For the cluster stacked surface mass density profile, we compute the covariance matrix  $C(r, r')$  using 10,000 bootstrap realisations, for each of the amplitude and redshift bins. As an illustrative case, in the left panel of Fig. 4 we display the normalised covariance matrix for one of the bin, specifically the bin with  $0.1 \leq z < 0.3$  and  $2.05 \leq A < 2.75$ , that contains 96 clusters. The central panel of Fig. 4 shows the normalised  $\Delta\Sigma$  covariance computed generating 10,000 times the AMICO-KiDS-DR3 cluster sample but assigning random positions in the KiDS-DR3 field-of-view. We notice that the off-diagonal term contributions in this case are almost negligible, which allows us to compute the final covariance  $CC(r, r')$  for the stacked excess surface mass density profiles, in each redshift and amplitude bins, by summing in quadrature the diagonal terms only:

$$CC(r, r') = C(r, r') \sqrt{1 + \frac{\delta(r, r') C^2(r, r')_{\text{Randoms}}}{n_{\text{Randoms}}^2 C^2(r, r')}} \quad (17)$$

with  $n_{\text{Randoms}} = 10,000$  and  $\delta(r, r')$  the two-dimensional delta Dirac function that is equal to one for  $r = r'$  and zero otherwise. The right panel of Fig. 4 shows the stacked  $\Delta\Sigma$  profile around the 96 clusters considered sample. The blue crosses (the orange circles) display the  $\sim 1h$ -case ( $1h + 2h$ -case) where the profiles are constructed adopting 14 (30) radial bins up to 3.16 Mpc/h (30 Mpc/h) minus the corresponding profiles around 10,000 random centre. The error bars represent the square-root of the diagonal term of the final covariance  $CC(r, r')$ . As an example, the red arrows, corresponding to each orange circle point, indicate the variation of the  $\Delta\Sigma$  profile.

In our analysis, performed adopting the CosmoBolognaLig (Marulli et al. 2016), we numerical invert the covariance matrix using the GSL<sup>3</sup> library.

Figure 4 shows that the random contribution at small scale is negligible, while it becomes relatively important at large scales when  $\Delta\Sigma$  is smaller than  $10 h M_{\odot}/\text{pc}^2$ . This justifies the choice by Bellagamba et al. (2019) not to correct for this effect in their small-scale analysis.

Figure 5 shows stacked excess surface mass density profiles of the AMICO-KiDS-DR3 clusters, divided in different ampli-

tude and redshift ranges. Blue and orange data points refer to the  $\sim 1h$  and  $1h + 2h$  data-set -cases, respectively. To both cases we subtract the contributions around random centres. The matching error bars display the square-root of the diagonal terms in the covariance matrix. Blue and red solid curves show the best-fit models, that is the median values of the posterior distributions assessed with the MCMC, corresponding to the  $\sim 1h$  and  $1h + 2h$  -cases, respectively. In running our MCMC on the  $\sim 1h$ -case data-set we adopt uniform priors for the 4 structural properties parameters, namely:

- $\log(M_{200}/h^{-1} M_{\odot})$ : [12.5 – 15.5];
- $c_{200}$ : [1 – 20];
- $f_{\text{off}}$ : [0 – 0.5];
- $\sigma_{\text{off}}/h^{-1} \text{Mpc}$ : [0 – 0.5].

## 4.2. Scaling Relations

In Fig. 6 we show the weak lensing mass-amplitude relation obtained in this work from the small-scale analysis ( $\sim 1h$ -case), compared to previous analysis performed on the same data-set. Moreover, we model the trend using a linear relation between the photometric observable and the recovered mass – as discussed also by Sereno & Ettori (2015) and Bellagamba et al. (2019):

$$\log \frac{M_{200}}{10^{14} M_{\odot}/h} = \alpha + \beta \log \frac{A}{A_{\text{piv}}} + \gamma \log \frac{E(z)}{E(z_{\text{piv}})}, \quad (18)$$

where we set  $A_{\text{piv}} = 2$ ,  $z_{\text{piv}} = 0.35$  as in Bellagamba et al. (2019) and  $E(z) = H(z)/H_0$ . We recall the reader that, differently from Bellagamba et al. (2019), we subtract the redshift stacked profiles around random centres and account for the full covariance matrix in our MCMC analysis. The red data points display the median results of our analysis, while the error bars show the 18th and 82nd percentiles of the posterior distributions. The black data points exhibit the original results by Bellagamba et al. (2019), with whom we obtain a reasonable agreement within the error bars. From the figure, though we notice that accounting for the full covariance in our MCMC analysis we obtain slightly smaller masses, and thus the slope of our linear relations (orange lines) is slightly shallower than the one derived by Bellagamba et al. (2019) (blue lines – we display the relation neglecting the redshift evolution in order to avoid overcrowding the figure). We have performed our analysis also accounting only for the  $1h$  term in the modelling function and adopting different cases for the

<sup>3</sup> <https://www.gnu.org/software/gsl>

**Table 2.** Scaling relation parameters of the mass-amplitude relation. The values reported are the median and 18th-82nd percentiles of the posterior distributions. The first line two lines show the results on the  $\sim 1h$ -case data-set adopting the full model (Eq. 15) or the one that account only for the  $1h$  term (Eq. 13) for constraining the cluster structural properties parameters. The third line exhibit the results modelling the  $1h + 2h$ -case data-set up to 35 Mpc/h.

case	$\alpha$	$\beta$	$\gamma$
$\sim 1h$	$0.097^{+0.019}_{-0.018}$	$1.943^{+0.098}_{-0.097}$	$0.904^{+0.615}_{-0.607}$
$\sim 1h$ (with $1h$ mod.)	$0.128^{+0.019}_{-0.017}$	$1.929^{+0.098}_{-0.099}$	$0.973^{+0.617}_{-0.624}$
$1h + 2h$	$0.096^{+0.017}_{-0.017}$	$1.912^{+0.085}_{-0.085}$	$0.950^{+0.552}_{-0.557}$

truncation radius. Particularly, we discuss in Appendix A the results adopting different truncation radii.

In Figure 7 we display the posterior distributions of the mass-amplitude model parameters (Eq. 18), obtained by modelling the red data points, and their corresponding error bars, shown in Fig. 6.

We follow the same fitting procedure adopted in Bellagamba et al. (2019), where the amplitude is computed through a lensing-weighted average. Moreover, we account for the systematic errors in the covariance by summing in quadrature the uncertainties for background selection, photo-zs and shear measurements Bellagamba et al. (2019); Sereno et al. (2020). We assume uniform priors in the range  $-1 < \alpha < 1$ ,  $0.1 < \beta < 5$  and  $-5 < \gamma < 5$ <sup>4</sup>. The obtained median values of the posterior distributions of the mass-amplitude relation parameters, and the 18th and 82nd percentiles around them, are summarised in Tab. 2. In the second line of the table we also report the scaling relation parameters for the masses estimated on the  $\sim 1h$ -case data-set but adopting in the modelling function only the  $1h$  term. In this case we notice that the slight overestimate of the masses drives the scaling relation toward a steeper value. We remind the reader to Table 1 where we display the median mass - expressed in term of the logarithm in base 10 - of the posterior distributions for the various cases considered; the values reported in parenthesis show the  $\chi^2$  divided by the number of degrees of freedom.

The contours in Fig. 7 display the 68th – 95th percentiles of the posterior distributions. For comparison, we show also the best-fit results obtained adopting a different parameterisation of the matter power spectrum in the 2-halo term (flat-WMAP9 parameters, but with  $\Omega_M = 0.3$  and  $h = 0.7$ ), and the results by Bellagamba et al. (2019). All results shown in Fig. 7 appear statistically consistent. We also notice and underline that the adoption of a flat- Planck18 or WMAP9 cosmology, fixing  $\Omega_M = 0.3$  and  $h = 0.7$ , impacts mainly in the modelling of the  $2h$  term that is negligible when analysing the  $\sim 1h$ -case data up to 3.16 Mpc/h.

As explained in Sec. 3.1, the 1-halo model used in this analysis has four free parameters:  $f_{\text{off}}$  and  $\sigma_{\text{off}}$ , that parameterise the uncertainty relative to the cluster centre definition, and  $M_{200}$  and  $c_{200}$ , which are related to the halo structural properties. Theoretical models (Eke et al. 2001; Zhao et al. 2009; Ludlow et al. 2012) and numerical simulations (Dolag et al. 2004; Neto et al. 2007; Macciò et al. 2008; Duffy et al. 2008; Klypin et al. 2014) predict that, at fixed redshift, the halo concentration is a decreasing function of the halo mass. Less massive haloes forming at higher redshifts tend to be more concentrated than the more massive ones (van den Bosch 2002; Wechsler et al. 2002); cluster size haloes are still in their formation phase.

<sup>4</sup> We use emcee for this fitting analysis, <https://emcee.readthedocs.io/en/stable>.

In Fig. 8 we display the concentration-mass relation for our stacked cluster sample in the three redshift bins considered, compared to the theoretical predictions for our reference cosmological model adopting the Zhao et al. (2009) recipe, where the concentration is related to the time at which haloes assemble 4% of their mass. To follow the mass accretion histories of the haloes back in time we use the model by Giocoli et al. (2012b). We perform a log-log linear regression modelling the 14 data points<sup>5</sup>, though the small number of data points does not allow us to constrain the redshift dependence of this relation.

The log-log linear relation obtained from the fitting analysis is the following:

$$\log c_{200} = B \log M_{200} + C, \quad (19)$$

with  $B = -0.22 \pm 0.21$  and  $C = 0.74 \pm 0.08$ , which is in good agreement with the results from numerical simulations (Duffy et al. 2008; Prada et al. 2012; Ludlow et al. 2014; Meneghetti et al. 2014) and from observational data Mandelbaum et al. (2008); Merten (2014); Sereno et al. (2017) in the corresponding mass ranges. The shaded light-magenta region encloses the  $1-\sigma$  uncertainties in both the slope and the intercept of the relation. For comparison and for each data point, the numbers exhibit the results for the  $c_{200} - M_{200}$  relation obtained adopting the truncation radius  $r_t$  equal to 1, 2 and 4 – in unit of  $R_{200}$ , respectively. In the figure, we also display with a dashed gold line the finding by Sereno et al. (2017) modelling the relation of the PSZ2LenS clusters and with a dot-dashed cyan one the results by Meneghetti et al. (2014) fitting the results of hydrodynamical simulations for the 2D fit of the X-ray selected cluster sample. Both relations refer to an intermediate redshift of our cluster sample corresponding to  $z = 0.35$ .

#### 4.3. Constraining the total matter density parameter

In this section we will present the results when modelling the large-scale  $\Delta\Sigma$  profiles up to 35 Mpc/h,  $1h + 2h$ -case. The large-scale signal is sensitive to the linear power spectrum normalisation and to the host halo bias (Sereno et al. 2015, 2017, 2018). In this work we follow the approach of fixing the halo bias-cluster mass relation – as well as its redshift dependence – to the results obtained from the analyses of various numerical simulations (Sheth & Tormen 1999; Sheth et al. 2001; Tinker et al. 2010) while leaving the matter density parameter  $\Omega_M$  as a free quantity to vary in our analysis. The  $\sigma_8$  parameter, measuring the power spectrum fluctuations smoothed with a top-hat window function of aperture 8 Mpc/h, will be obtained as a derived quantity from our MCMC and the corresponding cosmological model.

We employ the same Bayesian approach and the  $1h+2h$  modelling function used in the previous section, introducing an extra degree of freedom, that is the total matter density parameter  $\Omega_M$  – assuming a flat Universe, i.e.  $\Omega_\Lambda = 1 - \Omega_M$ . In doing so, we consistently account for the cosmology dependence of the conversion from angular to comoving and physical coordinate in our data-set – i.e. the radial profiles of  $\Delta\Sigma$ . The stacked weak lensing profiles shown before have been computed assuming a reference flat cosmology with  $\Omega_M = 0.3$  and  $h = 0.7$ . In the Bayesian analysis, when varying the matter density parameter, we take into account the dependence on  $\Omega_M$  not only on  $r$  but also on  $\Delta\Sigma$  (see Eq. 5).

<sup>5</sup> The fitting analysis is done with the Orthogonal Distance Regression routine <https://docs.scipy.org/doc/scipy/reference/odr.html>, accounting for the uncertainties in both mass and concentration.

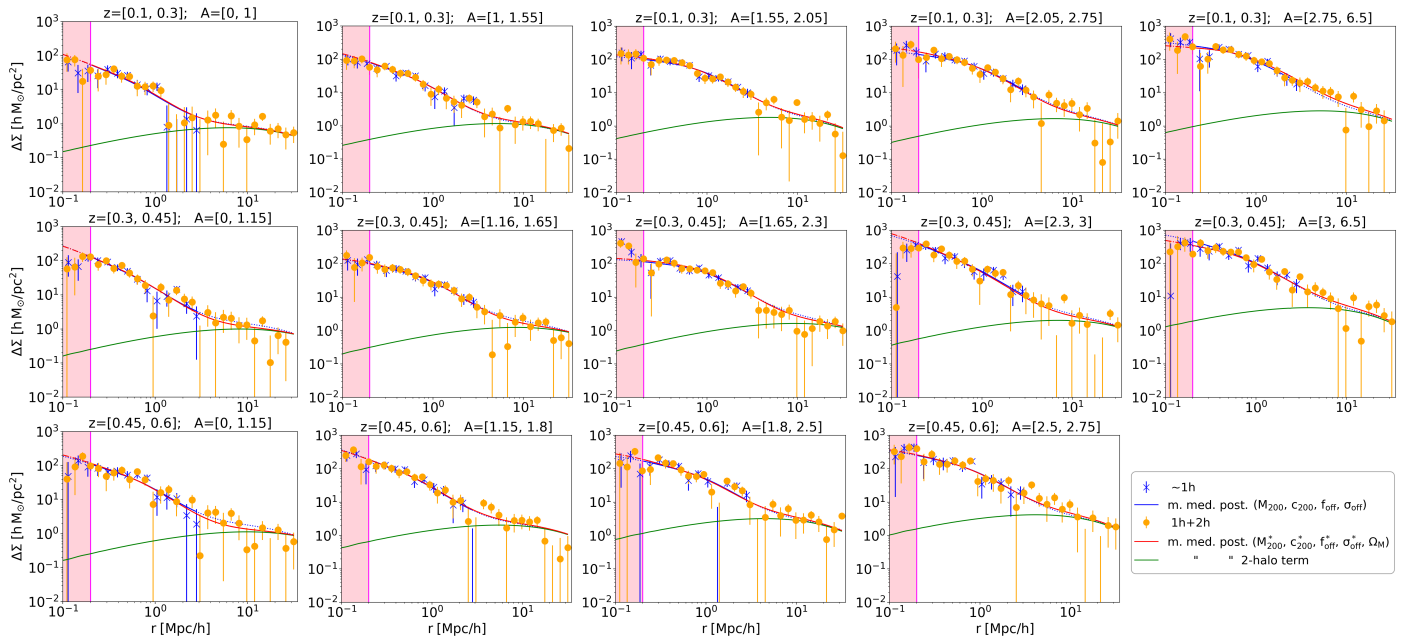


**Fig. 5.** Stacked excess surface mass density profiles of the clusters divided in different amplitude (from left to right) and redshift (from top to bottom) bins. Blue and orange data points refer to the  $\sim 1h$  and  $1h+2h$ -cases, respectively. The corresponding error bars represent the square-root of the diagonal terms in the corresponding covariance matrix. Blue and red solid curves show the best-fit models, that is the median values of the posterior distributions assessed with the MCMC, corresponding to the  $\sim 1h$  and  $1h+2h$ -cases, respectively. The blue and red curves are dotted and dashed outside the corresponding data-set, respectively; particularly the blue line below 0.2 and above 3.16 Mpc/h while the red only below 0.2 Mpc/h. The green curves show the 2-halo term contribution.

**Table 3.** Priors considered in the various redshift and amplitude bins. The different lines are ordered as in Tab. 1. For the halo structural properties (first four columns) we consider Gaussian priors with mean and standard deviations derived from the posteriors of the  $\sim 1h$ -case analysis, while for the total matter density parameter (last column) we assume a uniform prior.

–	$\log M_{200}$	$c_{200}$	$f_{\text{off}}$	$\sigma_{\text{off}}$	$\Omega_M$
1	$13.170 \pm 0.088$	$9.3 \pm 5.2$	$0.25 \pm 0.14$	$0.22 \pm 0.13$	[0.06 – 0.6]
2	$13.517 \pm 0.074$	$7.4 \pm 4.6$	$0.28 \pm 0.14$	$0.26 \pm 0.13$	" "
3	$14.034 \pm 0.059$	$2.7 \pm 1.3$	$0.27 \pm 0.14$	$0.24 \pm 0.14$	" "
4	$14.214 \pm 0.067$	$3.6 \pm 2.0$	$0.28 \pm 0.14$	$0.26 \pm 0.14$	" "
5	$14.507 \pm 0.065$	$5.2 \pm 2.1$	$0.31 \pm 0.14$	$0.20 \pm 0.10$	" "
6	$13.579 \pm 0.069$	$12.1 \pm 4.5$	$0.22 \pm 0.14$	$0.23 \pm 0.15$	" "
7	$13.835 \pm 0.073$	$4.2 \pm 3.1$	$0.29 \pm 0.14$	$0.29 \pm 0.13$	" "
8	$14.176 \pm 0.059$	$2.3 \pm 1.1$	$0.28 \pm 0.14$	$0.26 \pm 0.13$	" "
9	$14.255 \pm 0.082$	$12.0 \pm 4.5$	$0.24 \pm 0.14$	$0.26 \pm 0.15$	" "
10	$14.557 \pm 0.074$	$9.3 \pm 4.3$	$0.26 \pm 0.14$	$0.24 \pm 0.14$	" "
11	$13.664 \pm 0.088$	$7.5 \pm 4.8$	$0.29 \pm 0.14$	$0.24 \pm 0.12$	" "
12	$13.837 \pm 0.069$	$10.7 \pm 4.6$	$0.25 \pm 0.14$	$0.22 \pm 0.13$	" "
13	$14.143 \pm 0.082$	$4.9 \pm 3.4$	$0.29 \pm 0.14$	$0.29 \pm 0.14$	" "
14	$14.345 \pm 0.082$	$5.7 \pm 3.6$	$0.29 \pm 0.14$	$0.25 \pm 0.13$	" "

The red curves shown in Fig. 5 display the best-fit models computed from the MCMC Bayesian analysis, corresponding to the median values of the posterior distributions. As described in Sec. 3.2 and above, the considered model has five free parameters, that is  $M_{200}$ ,  $c_{200}$ ,  $f_{\text{off}}$ ,  $\sigma_{\text{off}}$  and  $\Omega_M$ . In modelling the  $1h+2h$ -case data-set we assume Gaussian priors for the four 1-halo model parameters with mean and standard deviation corresponding to the  $1h$ -case modelling posteriors, while we let  $\Omega_M$  vary between 0.06 and 0.6, uniformly (see Tab. 3). The green curves show the corresponding 2-halo term contribution.

In our analyses we decided to perform this twofold approach – first performing the fit of the halo structural property parameters and then, while limiting them to a smaller Gaussian interval, constraint the total matter density parameter – for two reasons. The first is related to the wide range of scales probed by our

stacked weak lensing profiles and the second is connected to the number of parameters that we vary – four for the 1-halo term and one for the 2-halo – our procedure allows separating in a self-consistent way the weights of the small and large scale contributions.

Fig. 9 displays the relation between the recovered weak lensing mass and total matter density parameter  $\Omega_M$ . From the figure, we note that there is no particular correlation. The data points display the medians and the error bars the 18th–82nd percentiles of the posterior distributions. The different coloured data points refer to the three redshift ranges considered. The blue solid vertical line and the cyan shaded region display the weighted average of the various  $\Omega_M$  estimates and its associated uncertainty.

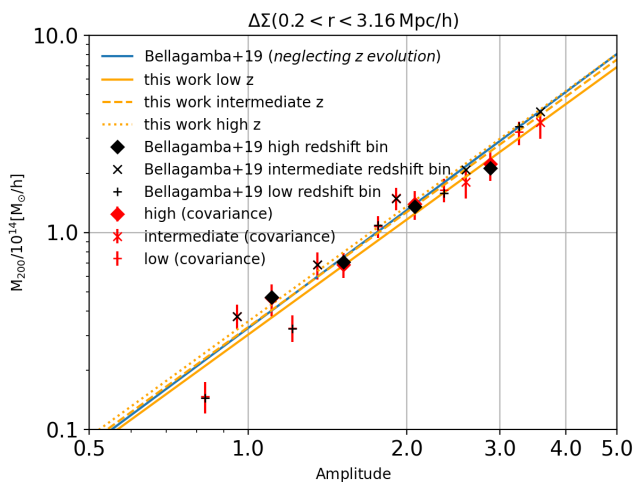


**Fig. 6.** Mass-amplitude relation obtained in the  $\sim 1h$ -case, accounting for the full covariance in each amplitude and redshift interval. We compare our results (red points) with the ones by Bellagamba et al. (2019) (black data points). The error bars show the 18th and 82nd percentiles of the posterior distributions. The blue solid line shows the scaling relation recovered by Bellagamba et al. (2019) while the orange ones exhibit our best fit result.

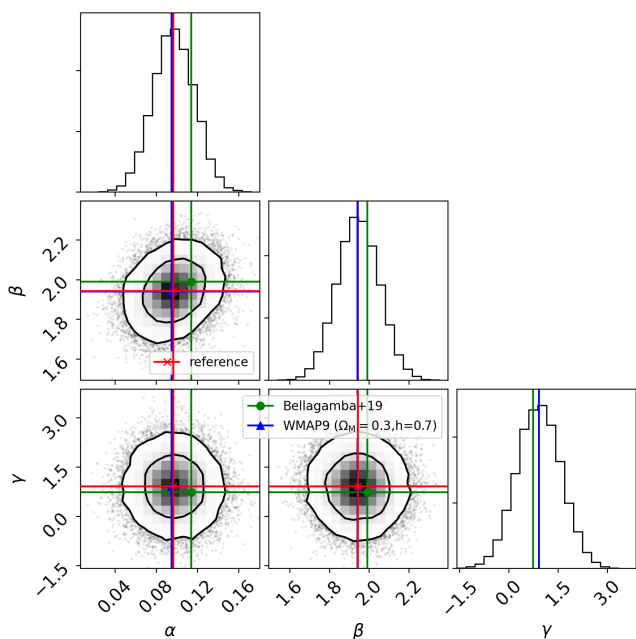


**Fig. 7.** Posterior distributions of the parameters of the mass-amplitude relation: Eq. 18. The contours show the 68th – 95th percentiles of the distributions. For comparison, we display also the results for  $\alpha$ ,  $\beta$  and  $\gamma$  obtained by Bellagamba et al. (2019) (green squares) and when assuming a flat WMAP9 cosmology, fixing  $\Omega_M = 0.3$  and  $h = 0.7$ .

The last line of Tab. 2 displays the mass-amplitude relation parameters (see Eq. 18) obtained modelling the  $1h + 2h$ -case data-set.

As discussed in Sec. 3, we assumed Planck18 as the reference cosmological model, but fixing  $\Omega_M = 0.3$  and  $h = 0.7$ , since the distances and the stacked weak lensing data have been computed assuming those parameters (Bellagamba et al. 2019). In Fig. 10 we show the posterior distributions for the measured  $\Omega_M$

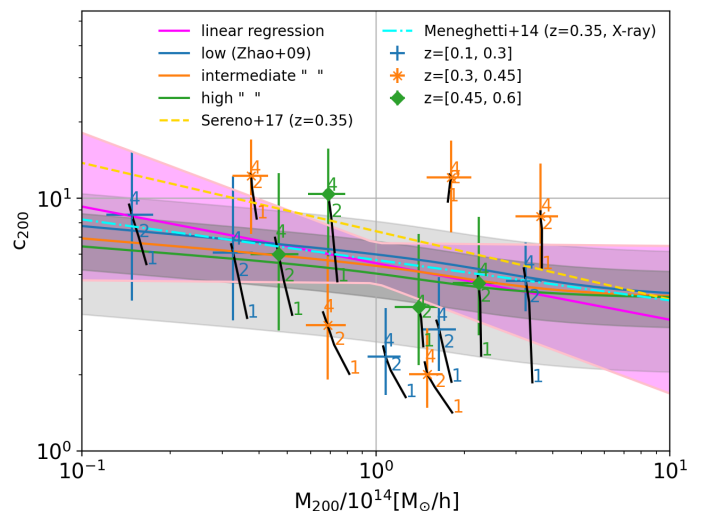


**Fig. 8.** Concentration-mass relation obtained from our stacked weak lensing analysis of the AMICO-KiDS-DR3 clusters. Data points and error bars show the median and the 18th–82th percentiles of the posteriors distributions. Blue, orange and green colours refer to the low, intermediate and high redshift cluster sub-samples. The solid curves represent the predictions by Zhao et al. (2009) in three redshift intervals. For each data point, the numbers show the results for the  $c - M$  relation obtained adopting the truncation radius  $r_t$  equal to 1, 2 and 4 – in unit of  $R_{200}$ , respectively. The gray and light-gray shaded regions indicate 1 and 2- $\sigma_{\ln c} = 0.25$  scatter as measured in numerical simulations (Dolag et al. 2004; Giocoli et al. 2012b). The magenta line shows the linear regression in the  $c - m$  relation computed using our reference results as data-set, while the shaded light-magenta region encloses the 1- $\sigma$  uncertainties in both the slope and the intercept of the relation. In this case, we use the ODR routine in python considering the uncertainties in both mass and concentration. Dashed gold and dash-dotted cyan display the results by Sereno et al. (2017) – based on observational data – and Meneghetti et al. (2014) – on hydrodynamical simulations, respectively.

parameter in the three redshift bins considered, as well as the result obtained by combining all redshifts together. In this case, we have fixed all the cosmological parameters to the flat Planck18 ones, varying only  $\Omega_M$  uniformly between  $[0.06 - 0.6]$ . The one halo term parameters are varied in the same range as done for the  $\sim 1h$ -case data-set, but assuming a Gaussian distribution for the priors with mean and standard deviation as from the  $\sim 1h$ -case posteriors. The solid black line exhibits the posterior distribution of  $\Omega_M$  from the analysis of the CMB data performed by the Planck Collaboration et al. (2020).

Table 4 reports the  $\Omega_M$  constraints obtained from the stacked weak lensing analyses at the three redshift ranges considered, and the combined one.

In our cosmological analysis, we are in good agreement with Lesci et al. (2020) and Nanni et al. (prep) who analysed the same AMICO-KiDS-DR3 data-set. This is remarkable since our analysis is independent from cluster-clustering and cluster-counts, but we still find a consistent value of  $\Omega_M$ .

We discuss the model systematics of our results in more details the two appendices. In Appendix A we examine the impact of the truncation radius in modelling the  $\sim 1h$ -case; while in Appendix B we discuss their impact in recovering the total matter density parameter – modelling the  $1h + 2h$ -case data-set, as well as the use of a different reference linear power spectra and various halo-bias models.

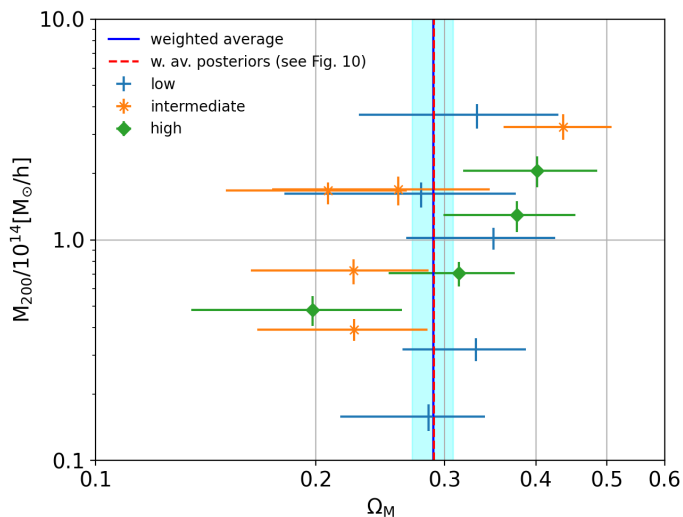


**Fig. 9.** Correlation between the recovered cluster mass and total matter density parameter from our stacked weak lensing analysis. The different coloured data points refer to three redshift ranges considered, as indicated in the legend. The blue solid line displays the weighted average of the various estimated  $\Omega_M$  the different amplitude and redshift bins; the cyan shaded region encloses the one  $\sigma$  uncertainty. The dashed red line exhibits the weighted average of the posterior distributions as in Fig. 10.

**Table 4.** Constraints on  $\Omega_M$  obtained from the stacked weak lensing analyses at the three redshift ranges considered, and the combined one.

	$\Omega_M$
all redshifts	$0.29 \pm 0.02$
low	$0.32 \pm 0.04$
intermediate	$0.26 \pm 0.03$
high	$0.31 \pm 0.04$

## 5. Summary & Conclusions

In this work, we presented new cosmological results from the analysis of weak lensing signal produced by a galaxy cluster sample detected from the KiDS-DR3 survey (de Jong et al. 2017; Hildebrandt et al. 2017). Specifically, we exploited photometric redshifts with relative probability distribution functions (Kuijken et al. 2015; de Jong et al. 2017), a global improved photometric calibration, weak lensing shear catalogues (Kuijken et al. 2015; Hildebrandt et al. 2017) and lensing-optimised image data. Our cluster sample, used to build the stacked shear profiles for the cosmological analysis, was obtained using the AMICO algorithm (Bellagamba et al. 2018) in Maturi et al. (2019). The redshift-amplitude binning of the cluster sample has been constructed as in Bellagamba et al. (2019).

Our studies support the use of the stacking method in weak lensing to calibrate galaxy cluster scaling relations, in agreement with previous results. The robustness of the AMICO-KiDS-DR3 data-set enabled us to infer cosmological parameters from the stacked shear measurements. Modelling the shear profiles of these clusters up to large scales, we inferred robust cosmological constraints on  $\Omega_M$ , assuming a reference recipe for the halo-bias parameter (Tinker et al. 2010).

We constructed two data-sets from the same cluster and galaxy shear catalogues. The first data-set has been used for the  $\sim 1h$ -case analysis, in which we binned the stacked radial excess surface mass density profiles in 14 intervals from 0.1 to 3.16 Mpc/h as in Bellagamba et al. (2019), while the second data-set

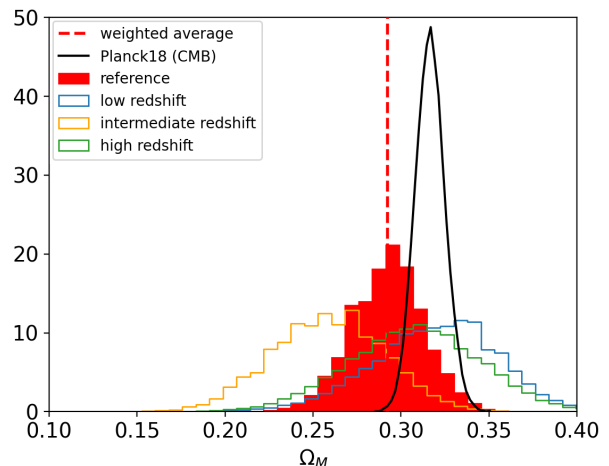


**Fig. 10.** Posterior distributions of the total matter density parameter  $\Omega_M$ . Blue, orange and green histograms show the results for the low, intermediate and high redshift cluster samples, respectively. The red-filled histogram exhibit the posterior distribution combining all redshifts together, the dashed red line indicates the median of the distribution. The black curve displays the posterior distribution obtained from the analysis of the CMB data by Planck Collaboration et al. (2020).

has been considered for the  $1h + 2h$ -case, where the analyses has been performed in 30 bins up to 35 Mpc/h. In order to keep under control all the observational systematic uncertainties of the survey, we subtracted to the measurements the signal around random centres, randomising 10,000 times the positions of the 6962 AMICO clusters. We also accounted for the full covariances on the final  $\Delta\Sigma$  profiles. We split our data-sets in 14 stacked measures in redshift and amplitude. We used a halo model approach developed in our MCMC routines in the CosmoBolognaLib (Marulli et al. 2016). Modelling the  $\sim 1h$ -case data-set, we recovered with good accuracy the cluster halo structural model parameters ( $M_{200}$ ,  $c_{200}$ ,  $f_{\text{off}}$ ,  $\sigma_{\text{off}}$ ) and the mass-amplitude relation parameters. We also studied the impact of adopting only the  $1h$  term in our modelling function, finding a small positive bias in mass of the order of few percents. In addition, we modelled the recovered concentration and mass relation of the 14 samples finding very good agreements with other observational studies and numerical simulation results: more massive haloes tend to be less concentrated than the smaller ones. However, the small data-set and the mild expected redshift dependence of the relation does not allow us to model the redshift evolution of the  $c_{200} - M_{200}$  relation.

We employed the  $1h + 2h$ -case data-set to simultaneously constrain the cluster structural properties and the  $\Omega_M$  parameter. Our results are fully consistent with the theoretical predictions of the  $\Lambda$ CDM model. Marginalising over the cluster model parameters, we obtained  $\Omega_M = 0.29 \pm 0.02$ , from the combined posterior distribution, assuming a flat geometry. This value is fully consistent with the independent results on the same cluster sample performed by Lesci et al. (2020) and Nanni et al. (prep), and also in agreement with the findings from recent CMB experiments (Bennett et al. 2013; Planck Collaboration et al. 2020). Higher than the low value of the total matter density parameter estimated from counts and weak lensing signal of redMaPPer clusters from the Dark Energy Survey (DES) Year 1 (?) and slightly lower than the one computed by Planck Collaboration et al. (2020) analysing CMB data.

We expect to reduce the uncertainties on our finding by enhancing the number of clusters to stack, looking forward to the new cluster catalogues from the future KiDS data releases, and afterwards from the data coming from future wide field surveys like the ESA-Euclid mission (Laureijs et al. 2011). In fact, upcoming deeper galaxy surveys will allow us to detect and stack lensing clusters in small redshift bins and to extend the analysis up to higher redshifts, enabling us to break parameter degeneracies and limit systematic uncertainties (Oguri & Takada 2011).

The accuracy in the estimate of cosmological parameters will significantly benefit from the advancements planned for KiDS when it will reach its final coverage of 1350 deg<sup>2</sup> of sky, with a median redshift of  $\sim 0.8$ .

The lensing signal can be incremented by considering a larger number of clusters (which can be attained with either deeper or wider surveys) and background sources (deeper surveys), and a wider survey area, in order to collect the 2-halo term lensing signal up to 50 Mpc/h. These aspects will be reached by ESA-Euclid mission, which will provide a significantly improved data-set compared to the one used in this work. The Euclid wide survey is expected to cover an area of  $\sim 15000$  deg<sup>2</sup> and it will detect approximately  $n_g \sim 30$  galaxies per square arcminute, with a median redshift larger than 0.9.

We conclude underling that our methodology of finding clusters, and our cosmological statistical analyses in modelling the weak lensing shear profiles around them, will represent a reference starting point and a milestone for cluster cosmology in near future experiments.

## Acknowledgments

Based on data products from observations made with ESO Telescopes at the La Silla Paranal Observatory under programme IDs 177.A-3016, 177.A-3017 and 177.A-3018, and on data products produced by Target/OmegaCEN, INAF-OACN, INAF-OAPD and the KiDS production team, on behalf of the KiDS consortium. OmegaCEN and the KiDS production team acknowledge support by NOVA and NWO-M grants. Members of INAF-OAPD and INAF-OACN also acknowledge the support from the Department of Physics & Astronomy of the University of Padova, and of the Department of Physics of Univ. Federico II (Naples). We acknowledge the KiDS collaboration for the pulic data realises and the various scientists working within it for the fruitful and helpful discussions. We acknowledge the grants ASI n.I/023/12/0, ASI-INAF n. 2018-23-HH.0 and PRIN MIUR 2015 Cosmology and Fundamental Physics: illuminating the Dark Universe with Euclid". CG and LM are also supported by PRIN-MIUR 2017 WSCC32 "Zooming into dark matter and proto-galaxies with massive lensing clusters". CG acknowledges support from the Italian Ministry of Foreign Affairs and International Cooperation, Directorate General for Country Promotion. MS acknowledges financial contribution from contract ASI-INAF n.2017-14-H.0 and contract INAF mainstream project 1.05.01.86.10. JHD acknowledges support from an STFC Ernest Rutherford Fellowship (project reference ST/S004858/1).

All authors have contributed to the scientific preparation of this work.

*Particularly:* CG has lead the paper preparing the data-set, performing the computational analyses and organising the manuscript; FM, LM, MS, AV and LG have helped with the development of some codes and the scientific interpretation of

the results; MM, MR, FB, MR have implemented the code for cluster detection and lead the first lensing analyses of the same data-set; SB, SC, GC, JHD, LI, GL, LN and EP participated to the discussion and interpretation of the results.

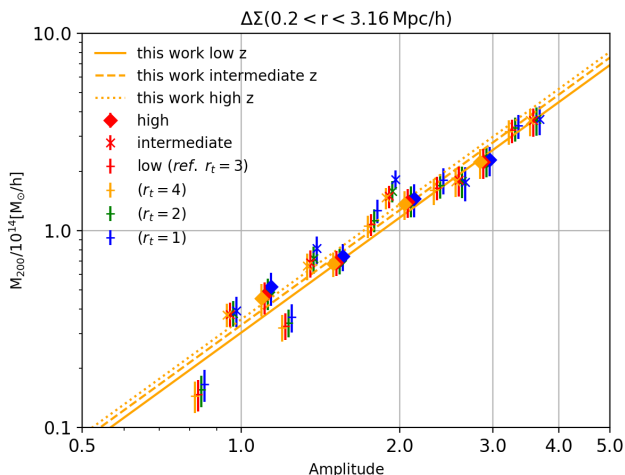


**Fig. A.1.** Mass-amplitude relation obtained using different modelling of the truncation radius; orange, green and blue refer to the cases with  $r_t = 4$ ,  $r_t = 2$  and  $r_t = 1$ , respectively. The red data points show the results for our reference model with  $r_t = 3$ . We slightly displace the data points along the x-direction, computed with different truncation radius definitions, to make the results more visible. The orange lines exhibit the best fit results for our reference case for the  $\sim 1h$ -case data-set as in the first line of Tab. 2.

**Table A.1.** Scaling relation parameters of the mass-amplitude relation. The values reported are the median and 18th-82nd percentiles of the posterior distributions. The different lines show the results on the  $\sim 1h$ -case data-set adopting different values of the truncation radius  $r_t$ .

case	$\alpha$	$\beta$	$\gamma$
$r_t = 1$	$0.138^{+0.019}_{-0.019}$	$1.902^{+0.102}_{-0.102}$	$0.904^{+0.615}_{-0.607}$
$r_t = 2$	$0.111^{+0.019}_{-0.019}$	$1.934^{+0.097}_{-0.098}$	$0.831^{+0.626}_{-0.617}$
$r_t = 4$	$0.090^{+0.019}_{-0.019}$	$1.949^{+0.097}_{-0.097}$	$0.906^{+0.618}_{-0.621}$

## Appendix A: Model systematics: 1h term

In this section we discuss the impact of different assumptions for the truncation radius in the  $1h$ -term modelling function of the projected density profile (see Eq. 9). As a first point, we examine the results modelling the  $\sim 1h$ -case data-set up to 3.16 Mpc/h and then discuss how the different assumptions impact on the total matter density parameter.

In Fig. A.1 we exhibit the mass-amplitude relation obtained using different values of the truncation radius:  $r_t=1, 2$  and 4, with respect to our reference case  $r_t = 3$  (red data points). The orange lines display the best fit results for our reference case as in Tab. 2. In our modelling function we include also the effect of the  $2h$  term for our reference cosmology (Planck18 with  $\Omega_M = 0.3$  and  $h = 0.7$ ) and assuming the Tinker et al. (2010) halo-bias relation. At fixed redshift and amplitude bin, the data points and the error bars show the median and the 18th – 82nd percentiles of the corresponding posterior  $M_{200}$  distributions. From the figure we notice a small trend – totally consistent within the uncertainties, and not always in the same direction – with the truncation radius: on average lower truncation radius slightly overestimate the mass. In Tab. A.1 we report the results of the mass-amplitude relations parameters (Eq. 18) for the different assumption on the  $r_t$  parameter. We notice that a lower truncation radius in the  $1h$  term model tends to produce a marginally steeper mass-amplitude relation. When the truncation radius varies from  $r_t = 1$ , to  $r_t = 4$  – in Eq. 18 – it changes from 0.138 to 0.090.

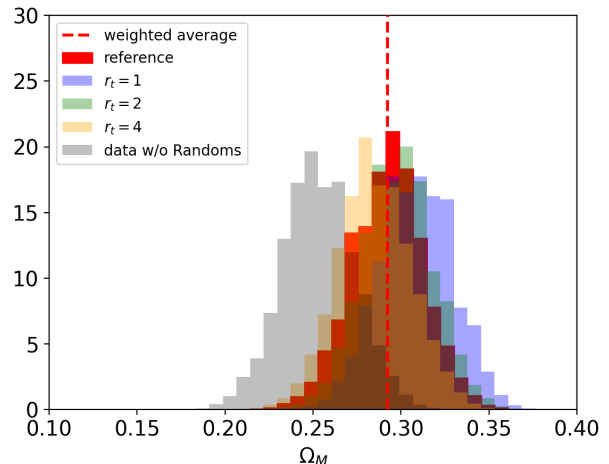


**Fig. B.1.** Combined posteriors, in redshift, for the recovered total matter density parameter assuming different values of the truncation radius. The red-filled histogram shows the posterior of our reference model with  $r_t = 3$ . Gold, green and blue histograms show the distributions of  $\Omega_M$  assuming  $r_t = 4, 2$  and 1, respectively. The gray histogram shows the result obtained from the stacked profiles estimated without accounting for the signal around random centres. The vertical red dashed line marks the weighted average of the reference posterior distribution.

## Appendix B: Model systematics: 2h term

In this section, we investigate how different model assumptions might affect also the recovered total matter density parameter. In Fig. B.1 we exhibit the combined posterior distributions, in redshifts, of  $\Omega_M$  obtained assuming different values of the truncation radius. We find a degeneracy between the effects of  $\Omega_M$  and the truncation radius, with a small value of the truncation radius being compensated by an increase of the total matter density parameter. Specifically, we find a systematic deviation of the total matter density parameter of the order of 5.6%, 2.1% and  $-2.5\%$  for  $r_t = 1, 2$  and 4 with respect to our reference case  $r_t = 3$ , respectively. In the same Figure we show also the result obtained from the stacked profiles estimated without accounting for the signal around random centres. In this case we get an underestimate  $\Omega_M$  of approximately 13%.

In Fig. B.2 we show the posterior distribution of the total matter density parameter assuming a linear power spectrum for the  $2h$  term adopting WMAP9 (Bennett et al. 2013) cosmological parameters with  $h = 0.7$ . The blue-filled histogram show the results combing all redshifts together, while red, orange and green histograms display the results for the low, intermediate and high redshift samples, respectively. We notice full consistency in our posterior distributions, particularly, when adopting a Planck18 or a WMAP9 cosmological parameters – and fixing  $h = 0.7$  – for the linear power spectrum when recovering  $\Omega_M$ . Using WMAP9 we slightly underestimate by 2% the total matter density parameter with respect to our reference case based on Planck18.

Considering that the normalisation of the 2-halo model depends on the halo bias parameter, we do expect our results to be dependent also on the assumed bias model. Figure B.3 shows the impact of different bias model assumptions on the  $\Omega_M$  posterior distributions. Assuming the Sheth & Tormen (1999) or Sheth et al. (2001) biasing models we obtain a weighted average of the combined posteriors for  $\Omega_M$  that is 3.5% and  $-3.2\%$  different

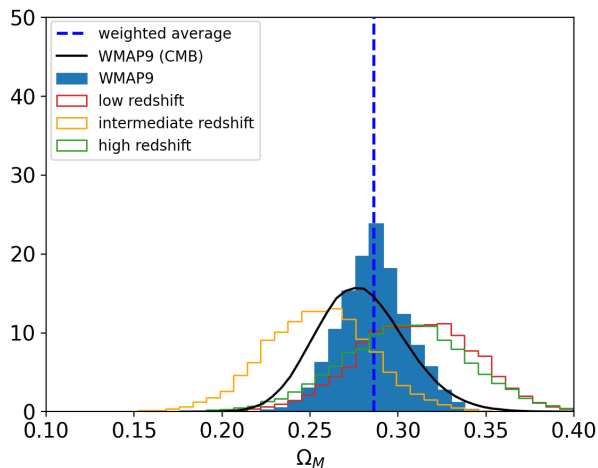


**Fig. B.2.** Posterior distributions of the total matter density parameter  $\Omega_M$ . Blue, orange and green histograms show the results for the low, intermediate and high redshift cluster samples, respectively. The red-filled histogram exhibit the posterior distribution combining all redshifts together, the dashed red line indicates the median of the distribution. The black curve displays the posterior distribution obtained from the analysis of the CMB data by [Bennett et al. \(2013\)](#).

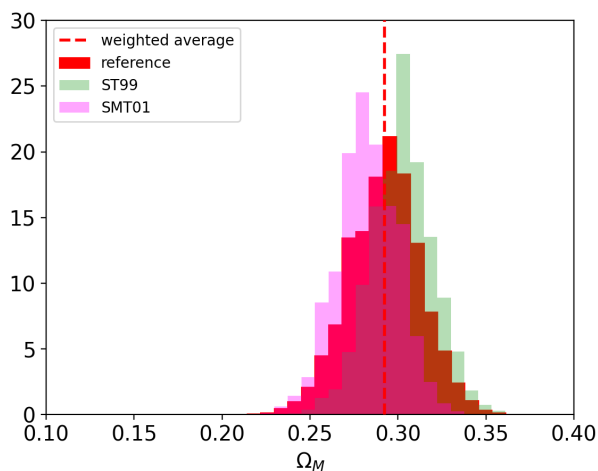


**Fig. B.3.** Combined posterior distributions obtained for different halo bias model. The red, gold and blue histograms show the cases obtained with [Tinker et al. \(2010\)](#) - our reference case, [Sheth & Tormen \(1999\)](#) and [Sheth et al. \(2001\)](#) halo biases, respectively.

than the one obtained with our reference model, based on the [Tinker et al. \(2010\)](#) halo-bias recipe.

The deviations observed when changing the cosmology, the bias model and the truncation radius are all comparable but smaller than the statistical error of our measurement. Those place some perspective on the systematics requirements for future data.

## References

Andreon S., 2010, *MNRAS*, 407, 263  
 Angelinelli M., Vazza F., Giocoli C., Ettori S., Jones T. W., Brunetti G., Brüggemann M., Eckert D., 2020, *MNRAS*, 495, 864  
 Angulo R. E., Springel V., White S. D. M., Jenkins a., Baugh C. M., Frenk C. S., 2012, *MNRAS*, 426, 2046  
 Baltz E. A., Marshall P., Oguri M., 2009, *J. Cosmology Astropart. Phys.*, 2009, 015

Bartelmann M., Schneider P., 2001, *Physics Reports*, 340, 291  
 Bautista J. E., Paviot R., Vargas Magaña M., de la Torre S., Fromenteau S., Gil-Marín H., et al. 2021, *MNRAS*, 500, 736  
 Bellagamba F., Maturi M., Hamana T., Meneghetti M., Miyazaki S., Moscardini L., 2011, *MNRAS*, 413, 1145  
 Bellagamba F., Roncarelli M., Maturi M., Moscardini L., 2018, *MNRAS*, 473, 5221  
 Bellagamba F., Sereno M., Roncarelli M., Maturi M., Radovich M., Bardelli S., Puddu E., Moscardini L., Getman F., Hildebrandt H., Napolitano N., 2019, *MNRAS*, 484, 1598  
 Benítez N., 2000, *ApJ*, 536, 571  
 Bennett C. L., Larson D., Weiland J. L., Jarosik N., Hinshaw G., Odegard N., Smith K. M., Hill R. S., et al. G., 2013, *ApJS*, 208, 20  
 Borgani S., Kravtsov A., 2011, *Advanced Science Letters*, 4, 204  
 Borgani S., Murante G., Springel G., Diaferio A., Dolag K., Moscardini L., Tormen G., Tornatore L., Tozzi P., 2004, *MNRAS*, 348, 1078  
 Cacciato M., Lahav O., van den Bosch F. C., Hoekstra H., Dekel A., 2012, *MNRAS*, 426, 566  
 Cacciato M., van den Bosch F. C., More S., Li R., Mo H. J., Yang X., 2009, *MNRAS*, 394, 929  
 Capaccioli M., Schipani P., 2011, *The Messenger*, 146, 2  
 Costanzi M., Rozo E., Simet M., Zhang Y., Evrard A. E., Mantz A., Rykoff E. S., Jeltema T., et al. 2019, *MNRAS*, 488, 4779  
 Covone G., Sereno M., Kilbinger M., Cardone V. F., 2014, *ApJ*, 784, L25  
 de Jong J. T. A., Verdoes Kleijn G. A., Boxhoorn D. R., Buddelmeijer H., Capaccioli M., Getman F., Grado A., et al. 2015, *A&A*, 582, A62  
 de Jong J. T. A., Verdoes Kleijn G. A., Erben T., Hildebrandt H., Kuijken K., Sikkema G., Brescia M., et al. 2017, *A&A*, 604, A134  
 de Jong J. T. A., Verdoes Kleijn G. A., Kuijken K. H., Valentijn E. A., 2013, *Experimental Astronomy*, 35, 25  
 Dolag K., Bartelmann M., Perrotta F., Baccigalupi C., Moscardini L., Meneghetti M., Tormen G., 2004, *A&A*, 416, 853  
 Duffy A. R., Schaye J., Kay S. T., Dalla Vecchia C., 2008, *MNRAS*, 390, L64  
 Eisenstein D. J., Hu W., 1999, *ApJ*, 511, 5  
 Eke V. R., Navarro J. F., Steinmetz M., 2001, *ApJ*, 554, 114  
 Fenech Conti I., Herbonnet R., Hoekstra H., Merten J., Miller L., Viola M., 2017, *MNRAS*, 467, 1627  
 George M. R., Leauthaud A., Bundy K., Finoguenov A., Ma C.-P., Rykoff E. S., Tinker J. L., Wechsler R. H., Massey R., Mei S., 2012, *ApJ*, 757, 2  
 Giocoli C., Bartelmann M., Sheth R. K., Cacciato M., 2010, *MNRAS*, 408, 300  
 Giocoli C., Meneghetti M., Bartelmann M., Moscardini L., Boldrin M., 2012a, *MNRAS*, 421, 3343  
 Giocoli C., Meneghetti M., Metcalf R. B., Ettori S., Moscardini L., 2014, *MNRAS*, 440, 1899  
 Giocoli C., Tormen G., Sheth R. K., 2012b, *MNRAS*, 422, 185  
 Hamana T., Shirasaki M., Miyazaki S., Hikage C., Oguri M., More S., Armstrong R., et al. 2020, *PASJ*, 72, 16  
 Hennig C., Mohr J. J., Zenteno A., Desai S., Dietrich J. P., Bocquet S., Strazzullo V., et al. 2017, *MNRAS*, 467, 4015  
 Heymans C., Van Waerbeke L., Miller L., Erben T., Hildebrandt H., Hoekstra H., Kitching T. D., et al. 2012, *MNRAS*, 427, 146  
 Hikage C., Oguri M., Hamana T., More S., Mandelbaum R., Takada M., Köhlinger F., et al. 2019, *PASJ*, 71, 43  
 Hildebrandt H., Erben T., Kuijken K., van Waerbeke L., Heymans C., Coupon J., Benjamin J., et al. 2012, *MNRAS*, 421, 2355  
 Hildebrandt H., Viola M., Heymans C., Joudaki S., Kuijken K., Blake C., Erben T., Joachimi B., et al. 2017, *MNRAS*, 465, 1454  
 Johnston D. E., Sheldon E. S., Wechsler R. H., Rozo E., Koester B. P., Frieman J. A., McKay T. A., Evrard A. E., Becker M. R., Annis J., 2007, *arXiv e-prints*, p. arXiv:0709.1159  
 Klypin A., Yepes G., Gottlober S., Prada F., Hess S., 2014, *ArXiv e-prints*  
 Kuijken K., 2011, *The Messenger*, 146, 8  
 Kuijken K., Heymans C., Hildebrandt H., Nakajima R., Erben T., de Jong J. T. A., Viola M., Choi A., et al. 2015, *MNRAS*, 454, 3500  
 Laureijs R., Amiaux J., Arduini S., Auguères J., Brinchmann J., Cole R., Cropper M., Dabin C., Duvet L., et al. 2011, *eprint arXiv: 1110.3193*  
 Lesci G. F., Marulli F., Moscardini L., Sereno M., Veropalumbo A., Maturi M., Giocoli C., Radovich M., Bellagamba F., Roncarelli M., Bardelli S., Contarini S., Covone G., Ingoglia L., Nanni L., Puddu E., 2020, *arXiv e-prints*, p. arXiv:2012.12273  
 Lewis A., Challinor A., Lasenby A., 2000, *Astrophys. J.*, 538, 473  
 Liske J., Baldry I. K., Driver S. P., Tuffs R. J., Alpaslan M., Andrae E., Brough S., Cluver M. E., et al. 2015, *MNRAS*, 452, 2087  
 LSST Science Collaboration Abell P. A., Allison J., Anderson S. F., Andrew J. R., Angel J. R. P., Armus L., Arnett D., Asztalos S. J., Axelrod T. S., et al. 2009, *eprint arXiv: 0912.0201*  
 Ludlow A. D., Navarro J. F., Angulo R. E., Boylan-Kolchin M., Springel V., Frenk C., White S. D. M., 2014, *MNRAS*, 441, 378

- Ludlow A. D., Navarro J. F., Li M., Angulo R. E., Boylan-Kolchin M., Bett P. E., 2012, *MNRAS*, 427, 1322
- Macciò A. V., Dutton A. A., van den Bosch F. C., 2008, *MNRAS*, 391, 1940
- Macciò A. V., Dutton A. A., van den Bosch F. C., Moore B., Potter D., Stadel J., 2007, *MNRAS*, 378, 55
- Mandelbaum R., Hirata C. M., Ishak M., Seljak U., Brinkmann J., 2006, *MNRAS*, 367, 611
- Mandelbaum R., Seljak U., Hirata C. M., 2008, *J. Cosmology Astropart. Phys.*, 2008, 006
- Mandelbaum R., Slosar A., Baldauf T., Seljak U., Hirata C. M., Nakajima R., et al. 2013, *MNRAS*, 432, 1544
- Marulli F., Veropalumbo A., García-Farieta J. E., Moresco M., Moscardini L., Cimatti A., 2020, arXiv e-prints, p. arXiv:2010.11206
- Marulli F., Veropalumbo A., Moresco M., 2016, *Astronomy and Computing*, 14, 35
- Marulli F., Veropalumbo A., Sereno M., Moscardini L., Pacaud F., Pierre M., Plionis M., Cappi A., et al. 2018, *A&A*, 620, A1
- Maturi M., Bellagamba F., Radovich M., Roncarelli M., Sereno M., Moscardini L., Bardelli S., Puddu E., 2019, *MNRAS*, 485, 498
- Maturi M., Meneghetti M., Bartelmann M., Dolag K., Moscardini L., 2005, *A&A*, 442, 851
- Maturi M., Schirmer M., Meneghetti M., Bartelmann M., Moscardini L., 2007, *A&A*, 462, 473
- Meneghetti M., Rasia E., Merten J., Bellagamba F., Ettori S., Mazzotta P., Dolag K., Marri S., 2010b, *A&A*, 514, A93+
- Meneghetti M., Rasia E., Vega J., Merten J., Postman M., Yepes G., Sembolini F., Donahue M., Ettori S., Umetsu K., Balestra I., et al. 2014, *ApJ*, 797, 34
- Merten J., 2014, ArXiv e-prints
- Miller L., Heymans C., Kitching T. D., van Waerbeke L., Erben T., Hildebrandt H., Hoekstra H., et al. 2013, *MNRAS*, 429, 2858
- Miller L., Kitching T. D., Heymans C., Heavens A. F., van Waerbeke L., 2007, *MNRAS*, 382, 315
- Mo H. J., White S. D. M., 1996, *MNRAS*, 282, 347
- Moresco M., Veropalumbo A., Marulli F., Moscardini L., Cimatti A., 2020, arXiv e-prints, p. arXiv:2011.04665
- Murata R., Oguri M., Nishimichi T., Takada M., Mandelbaum R., More S., et al. 2019, *PASJ*, 71, 107
- Nanni L., et al., in prep.
- Navarro J. F., Frenk C. S., White S. D. M., 1997, *ApJ*, 490, 493
- Neto A. F., Gao L., Bett P., Cole S., Navarro J. F., Frenk C. S., White S. D. M., Springel V., Jenkins A., 2007, *MNRAS*, 381, 1450
- Oguri M., Hamana T., 2011, *MNRAS*, 414, 1851
- Oguri M., Takada M., 2011, *Phys. Rev. D*, 83, 023008
- Pacaud F., Pierre M., Melin J. B., Adami C., Evrard A. E., Galli S., Gastaldello et al. 2018, *A&A*, 620, A10
- Planck Collaboration 2016, *Astron. Astrophys.*, 594, A13
- Planck Collaboration Ade P. A. R., Aghanim N., Alves M. I. R., Armitage-Caplan C., Arnaud M., Ashdown M., Atrio-Barandela F., Aumont J., Aussel H., et al. 2014, *A&A*, 571, A1
- Planck Collaboration Ade P. A. R., Aghanim N., Arnaud M., Ashdown M., Aumont J., Baccigalupi C., Banday A. J., Barreiro R. B., Bartlett J. G., et al. 2016, *A&A*, 594, A24
- Planck Collaboration Aghanim N., Akrami Y., Ashdown M., Aumont J., Baccigalupi C., Ballardini M., et al. 2020, *A&A*, 641, A6
- Prada F., Klypin A. A., Cuesta A. J., Betancort-Rijo J. E., Primack J., 2012, *MNRAS*, 423, 3018
- Radovich M., Puddu E., Bellagamba F., Roncarelli M., Moscardini L., Bardelli S., Grado A., Getman F., Maturi M., Huang Z., Napolitano N., McFarland J., Valentijn E., Bilicki M., 2017, *A&A*, 598, A107
- Rasia E., Borgani S., Ettori S., Mazzotta P., Meneghetti M., 2013, *ApJ*, 776, 39
- Rasia E., Meneghetti M., Martino R., Borgani S., Bonafede A., Dolag K., Ettori S., Fabjan D., Giocoli C., Mazzotta P., Merten J., Radovich M., Tornatore L., 2012, *New Journal of Physics*, 14, 055018
- Sartoris B., Biviano A., Fedeli C., Bartlett J. G., Borgani S., Costanzi M., Giocoli C., Moscardini L., Weller J., Ascaso B., Bardelli S., Maurogordato S., Viana P. T. P., 2016, *MNRAS*, 459, 1764
- Sereno M., Covone G., Izzo L., Ettori S., Coupon J., Lieu M., 2017, *MNRAS*, 472, 1946
- Sereno M., Ettori S., 2015, *MNRAS*, 450, 3675
- Sereno M., Ettori S., Lesci G. F., Marulli F., Maturi M., Moscardini L., Radovich M., Bellagamba F., Roncarelli M., 2020, *MNRAS*, 497, 894
- Sereno M., Giocoli C., Izzo L., Marulli F., Veropalumbo A., Ettori S., Moscardini L., Covone G., Ferragamo A., Barrena R., Streblyanska A., 2018, *Nature Astronomy*, 2, 744
- Sereno M., Veropalumbo A., Marulli F., Covone G., Moscardini L., Cimatti A., 2015, *MNRAS*, 449, 4147
- Sheldon E. S., Johnston D. E., Scranton R., Koester B. P., McKay T. A., Oyaizu H., Cunha C., Lima M., Lin H., Frieman J. A., Wechsler R. H., Annis J., Mandelbaum R., Bahcall N. A., Fukugita M., 2009, *ApJ*, 703, 2217
- Sheth R. K., Mo H. J., Tormen G., 2001, *MNRAS*, 323, 1
- Sheth R. K., Tormen G., 1999, *MNRAS*, 308, 119
- Simet M., McClintock T., Mandelbaum R., Rozo E., Rykoff E., Sheldon E., Wechsler R. H., 2017, *MNRAS*, 466, 3103
- Spergel D., Gehrels N., Breckinridge J., Donahue M., Dressler A., Gaudi B. S., Greene T., Guyon O., Hirata C., et al. K., 2013, eprint arXiv: 1305.5422
- Springel V., White S. D. M., Tormen G., Kauffmann G., 2001b, *MNRAS*, 328, 726
- Tinker J. L., Robertson B. E., Kravtsov A. V., Klypin A., Warren M. S., Yepes G., Gottlöber S., 2010, *ApJ*, 724, 878
- Tormen G., 1998, *MNRAS*, 297, 648
- Umetsu K., 2020, *A&A Rev.*, 28, 7
- van den Bosch F. C., 2002, *MNRAS*, 331, 98
- Veropalumbo A., Marulli F., Moscardini L., Moresco M., Cimatti A., 2014, *MNRAS*, 442, 3275
- Veropalumbo A., Marulli F., Moscardini L., Moresco M., Cimatti A., 2016, *MNRAS*, 458, 1909
- Vikhlinin A., Kravtsov A. V., Burenin R. A., Ebeling H., Forman W. R., Hornstrup A., Jones C., Murray et al. 2009, *ApJ*, 692, 1060
- Viola M., Cacciato M., Brouwer M., Kuijken K., Hoekstra H., Norberg P., Robotham A. S. G., et al. 2015, *MNRAS*, 452, 3529
- Viola M., Maturi M., Bartelmann M., 2010, *MNRAS*, 403, 859
- Wechsler R. H., Bullock J. S., Primack J. R., Kravtsov A. V., Dekel A., 2002, *ApJ*, 568, 52
- Yang X., Mo H. J., van den Bosch F. C., Jing Y. P., Weinmann S. M., Meneghetti M., 2006, *MNRAS*, 373, 1159
- Zenteno A., Mohr J. J., Desai S., Stalder B., Saro A., Dietrich J. P., Bayliss M., Bocquet S., Chiu I., Gonzalez A. H., Gangkofner C., Gupta N., Hlavacek-Larrondo J., McDonald M., Reichardt C., Rest A., 2016, *MNRAS*, 462, 830
- Zhang Y., Miller C., McKay T., Rooney P., Evrard A. E., Romer A. K., Perfecto R., Song J., et al. 2016, *ApJ*, 816, 98
- Zhao D. H., Jing Y. P., Mo H. J., Bnörner G., 2009, *ApJ*, 707, 354